BANDWIDTH ENHANCEMENT OF DIELECTRIC RESONATOR ANTENNAS

Richard Q. Lee* and Rainee N. Simons
NASA Lewis Research Center
MS 54-8
Cleveland, Ohio 44135

ABSTRACT

This paper reports an experimental investigation of bandwidth enhancement of dielectric resonator antennas (DRA) using parasitic elements. Substantial bandwidth enhancement for the $HE_{11\delta}$ mode of the stacked geometry and for the $HE_{13\delta}$ mode of the coplanar collinear geometry have been demonstrated. Excellent radiation patterns for the $HE_{11\delta}$ mode were also recorded.

INTRODUCTION

A dielectric resonator placed over a ground plane can serve as an effective radiator [1-2]. Compared to printed antennas, the DRA has lower ohmic losses and higher radiation efficiency particularly at high frequencies. However, because of high Q factor, the DRA has very narrow bandwidth which severely limits its usefulness as an antenna. It has been demonstrated that significant bandwidth enhancement can be achieved for microstrip antennas by placing closely spaced parasitic elements on both sides of or directly above a driven patch [3]. It appears that parasitic elements can also be used to enhance the bandwidth of a DRA. This paper is concerned with an experimental investigation of the effects of parasitic elements on dielectric resonator antennas.

THE EXPERIMENT

The single DRA as shown in Fig. 1(a) is placed on a ground plane and aperture coupled to a notched coplanar waveguide (CPW) through a slot. The slot is positioned along the y-axis (ϕ=90°) so the $HE_{11\delta}$ and the $HE_{13\delta}$ modes can be excited [4]. Bond wires are used to keep the CPW ground planes at equal potential and suppress the slotline even mode. The DRA of diameter D and height H of 6.223 mm and 2.489 mm respectively is constructed from $ZrSnTiO_4$ material of relative permittivity $\epsilon_{r2} \simeq 36.0$, and the CPW feed is fabricated from 20 mil (0.508 mm) RT-5880 Duroid substrate of $\epsilon_{r1} = 2.2$. In the experiment, identical dielectric resonators were placed directly above and on both sides of the driven DRA.

RESULTS AND DISCUSSIONS

The measured return losses for the single DRA is shown in Fig. 2(a). Results indicate that with proper aperture lengths, either the $HE_{11\delta}$ or the $HE_{13\delta}$ mode can be strongly excited. The aperture length was found to have a strong impact on the bandwidth of the DRA. The $HE_{11\delta}$ mode excited with an aperture L_1 = 0.40 cm has a 2:1 VSWR bandwidth of 8.8 %, while the $HE_{13\delta}$ excited with an aperture L_1 = 0.68 cm has a bandwidth of only 2.5 %.The return losses are less than -10 dB for both modes indicating strong coupling. Figure 3(a) shows the measured patterns for the $HE_{11\delta}$ which has a broader main lobe in the ϕ=90° plane than in the ϕ=0° plane. The pattern is asymmetrical along the ϕ=0° plane due to interference from the test fixture.

Figure 1(b) shows the collinear geomtry where two identical dielectric resonators are proximity coupled to a driven DRA along the ϕ=0° plane with one on each side of the DRA. The separation between resonators is 1 mm. It was observed that placing the parasitic dielectric along the ϕ=0° plane produces strong coupling with the $HE_{13\delta}$ mode, while along the ϕ=90° plane produces strong coupling with the $HE_{11\delta}$ mode. The strong coupling is caused by high field concentrations of the $HE_{13\delta}$ and $HE_{11\delta}$ in the ϕ=0° and ϕ=90° plane respectively. Figure 2(b) shows the measured return losses which are less than -18 dB for the $HE_{13\delta}$ mode with ϕ=o° orientation and about -50 dB for the $HE_{11\delta}$ with ϕ=90° orientation. The parasitic elements has increased the 2:1 VSWR bandwidth of the $HE_{13\delta}$ from 2.5 % to 3.7 %. The measured patterns for the $HE_{11\delta}$ mode as shown in Fig. 3(b) exhibits excellent broadside characteristics.

Figure 1(c) shows the stacked geomtry. The overlaying parasitic resonator was found to couple strongly to the $HE_{11\delta}$ mode where the electric field is maximum near the top surface of the driven DRA [6]. As indicated in Fig. 2(c), the measured return loss is less than -20 dB for the $HE_{11\delta}$ mode with the higher order mode sup- pressed. The parasitic resonator increases the 2:1 VSWR bandwidth of the $HE_{11\delta}$ mode to over 5.3 %. As with the previous case, excellent radiation patterns have been obtained for the $HE_{11\delta}$ mode. These patterns are displayed in Fig. 3(c).

CONCLUSIONS

Substantial enhancement in bandwidth has been demonstrated for the HE_{11} and the HE_{13} modes with the parasitic resonators placed directly above and on both sides of the DRA respectively. Because of excellent

return loss and radiation characteristics, the DRA should be excited in HE_{11} mode when used as radiating elements in an array.

REFERENCES

[1] S.A. Long, M.W. Mcallister and L.C. Shen, "The resonant cylindrical dielectric cavity antenna," IEEE Trans. Ant. & Prog., Vol.AP-31, No.3, PP.406-412, May 1983.

[2] J.T.H. St.-Martin, Y.M.M. Antar, A.A. kishk, A. Ittipiboon, and M. Cuhaci, "Dielectric resonator antenna using aperture coupling," Electron. Lett. Vol.26, No.24, pp.2015-2016, Nov. 1990.

[3] R.Q. Lee, K.F. Lee anf J. Bobibchak, "Characteris tics of a two-layer electromagnetically coupled rectangular patch antenna," Electron. Lett., Vol.28, No.1, pp.75-76, Jan. 92.

[4] D. Kajfez, A.W. Glisson and J. James, "Computed model field distributions for isolated dielectric resonators," IEEE Trans. Microwave Theory tech., Vol.MTT-32, No.12, pp.1609-1616, Dec. 1984.

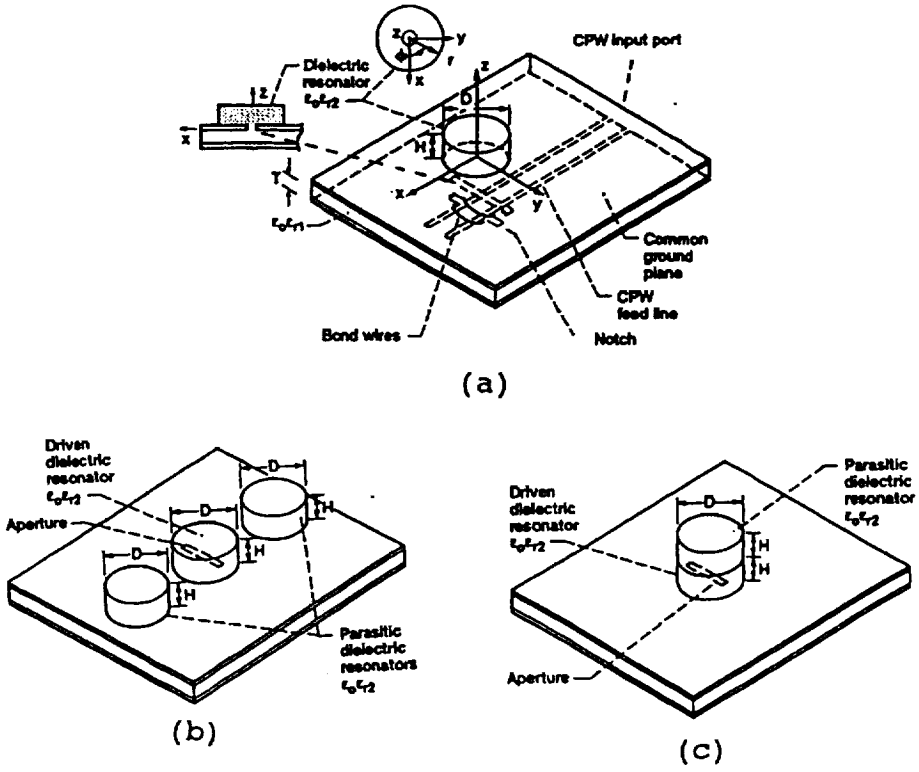

Fig. 1 Schematic Illustrating a Grounded Dielectric Resonator Aperture Coupled to a Notched CPW feed: (a) Single , (b) multiple and (c) Stacked Dielectric Resonator Antenna.

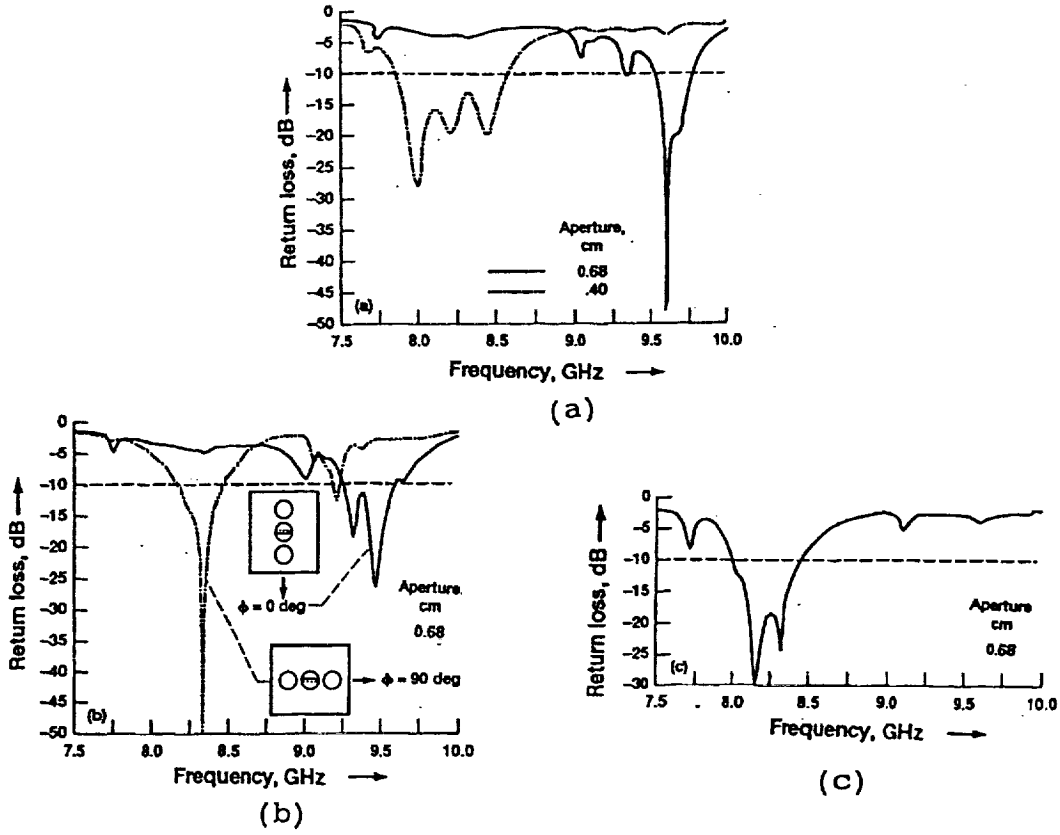

Fig. 2 Measured Return Losses for: (a) Single, (b) Multiple and (c) Stacked Dielectric Resonator Antenna.

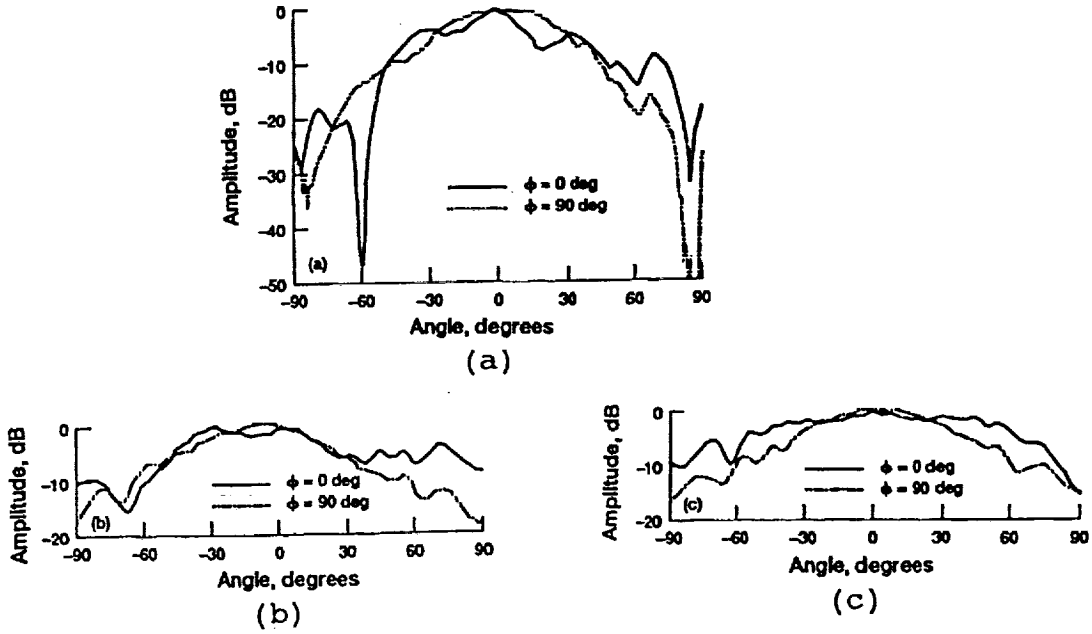

Fig. 3 Measured Radiation Patterns for the $HE_{11\delta}$ Mode for: (a) Single, (b) Multiple and (c) Stacked Dielectric resonator Antenna (f= 8.2 GHz).

SPACE POWER AMPLIFICATION WITH ACTIVE LINEARLY TAPERED SLOT ANTENNA ARRAY

Rainee N. Simons and Richard Q. Lee

National Aeronautics and Space Administration
Lewis Research Center
Cleveland, Ohio 44135

Abstract

A space power amplifier composed of active linearly tapered slot antennas (LTSAs) has been demonstrated and shown to have a gain of 30 dB at 20 GHz. In each of the antenna elements, a GaAs monolithic microwave integrated cir-cuit (MMIC) three-stage power amplifier is integrated with two LTSAs. The LTSA and the MMIC power amplifier have a gain of 11 dB and power added efficiency of 14 percent respectively. The design is suitable for constructing a large array using monolithic integration techniques.

Introduction

The power output as well as the dynamic range of microwave solid state devices decreases as the frequency of operation increases. Hence to obtain high power at fundamental frequencies of several tens of GHz, the output from all the devices have to be combined using either conventional power combiners or quasi-optical power combiners.[1] In the case of conventional power combiners, the combining is done with Wilkinson, radial line, and hybrid coupled networks. In the case of quasi-optical combiners, oscillators constructed with IMPATT diodes,[2] Gunn diodes,[3] MESFETs,[4] or HEMTs[5] are integrated with microstrip patch antennas or linearly tapered slot antennas (LTSAs)[6] to form an active antenna array which combines power radiatively in free space. The advantages of quasi-optical power combiners over conventional power combiners are higher combining efficiency because of lower conductor losses and larger dimensional tolerances with the absence of resonance modes. In addition both antennas and devices can be integrated on a single semiconductor wafer thus simplifying the array construction. The disadvantage of oscillator based quasi-optical combiners is that the individual oscillators have to be phase locked to a reference source or the active array has to be placed in a Fabry-Perot resonator to produce coherent radiation.

Another way to obtain high power is to construct a spatial amplifier. One such scheme is the grid amplifier.[7] Each unit cell of the grid amplifier consists of a pair of packaged GaAs MESFETs with the sources connected together to form a differential amplifier and with the gate and drain terminals extending radially to form a pair of orthogonal strip antennas. Radiation to and from a planar array of identical unit cells is quasi-optically coupled by a vertically or a horizontally polarized beam respectively.

This paper presents for the first time a spatial amplifier with GaAs monolithic microwave integrated circuit (MMIC) multi-stage power amplifiers. In this approach an array of active antenna modules constructed from nonplanar LTSAs[8] and GaAs MMIC amplifiers receives signals at lower power, and after amplification re-radiates signals into free space. The two advantages of the spatial amplifier over the spatial oscillator are that only a single stable lower power source is required (thus greatly simplifying the combiner construction) and that the amplifiers can be individually optimized. Figure 1 schematically illustrates a possible arrangement for space power amplification.

Active Antenna Module Characteristics

The experimental three-element array module is showns chematically in Figure 2. The array elements are constructed by integrating a GaAs MMIC multi-stage power amplifier between two nonplanar LTSAs.

Linearly Tapered Slot Antenna

The feed system of the nonplanar LTSA consists of a conventional microstrip with the ground plane tapered to form a balanced microstrip. The strip conductors of the balanced microstrip are gradually flared with respect to the antenna axis to form the nonplanar LTSA. The design of the non-planar LTSA and its characteristics are reported in Ref. 8. The antenna is fabricated on a 0.02 inch thick RT-5880 Duroid substrate. The measured gain of the LTSA is about 11 dB at the center frequency of 20 GHz. The LTSA has a return loss S_{11} of 10 dB (2:1 VSWR) over a bandwidth extending from 10 to 30 GHz.

GaAs MMIC Multi-Stage Power Amplifier

The GaAs MMIC three-stage power amplifier was designed and fabricated by Texas Instruments for NASA Lewis Research Center.[9] A photograph of the amplifier chip is shown in Figure 3. The amplifier is constructed on a GaAs substrate with an active layer doping level of 2.5×10^{17} cm^{-3}. The gate widths of the three stages are 1.2, 2.4, and 6.0 mm, respectively, and the gate length is 0.5 μm in all the stages. The chip size is about 4.0 by 3.0 by 0.1 mm. The bias network is incorporated on the chip. The drain voltage V_d and current I_d is 6.3 V and 1.9 A, respectively. The gate voltage

V_g is -0.6 V. The measured gain (S_{21}) on a HP 8510B ANA with a 40 dB coaxial attenuator on the drain side of a typical amplifier is shown in Figure 4. The gain is greater than 10 dB over the frequency range of 18 to 21 GHz. The saturated output power measured on a Pacific Instruments scalar network analyzer at 20 GHz is about 1.8 W with a gain of 10 dB and power added efficiency of 14 percent.[9]

Experimental Results and Discussions

A simple measurement procedure has been developed to estimate the gain of the space amplifier. This procedure involves the LTSAs at the input terminals are space fed from a single horn antenna while those at the output terminals radi-ate into free space. The free space radiation is picked up by a second horn antenna which is placed at a far field distance from the array. The ratio of the measured received power with and without bias to the MMIC amplifiers provides an estimate of the gain of the space amplifier. In the setup, the two horn antennas are orthogonally polarized but the LTSAs are oriented to have the same polarization as their respective horn antennas, thus good isolation between the transmitting and the receiving horn antennas is established. Also, for comparison purposes, a single LTSA was tested as a receive antenna. The H-plane pattern is shown in Figure 5 which exhibits a power gain of 6.7 dB with the MMIC amplifier turned ON.

Three-Element Array Module

In this experiment, the LTSAs at the amplifier input and output are oriented with the H and E vectors of the receiving horn, respectively as shown in Figure 6(a). This arrange-ment allows the horn to excite the three LTSAs with equal amplitude. The measured radiation pattern is shown in Figure 7(a) with the amplifiers turned ON and OFF, respectively. The gain increases by as much as 30 dB when the amplifiers are turned ON which is in good agreement withthe measured gain of the amplifiers.

A second experiment, as shown in Figure 6(b), is carried out with the LTSAs at the input and output oriented with the H and E vectors of the receiving horn, respectively. The measured radiation pattern is shown in Figure 7(b). In this arrangement the gain increases by 25 dB when the amplifiers are turned ON. The gain is lower in this case because the LTSAs on either side of the center element are excited with a lower amplitude due to the amplitude taper of the electric field distribution of the transmitting horn. The experimental three element LTSA MMIC array module is shown in Figure 8.

Conclusions

A space power amplifier composed of active LTSA antennas has been demonstrated and shown to have a gain of 30 dB at 20 GHz. In each of the antenna elements, a MMIC three-stage power amplifier is integrated with two LTSAs. The GaAs MMIC power amplifier and the LTSA have a power added efficiency of 14 percent and a gain of 11 dB, respectively. The design is suitable for constructing a large array using monolithic integration techniques.

References

1. K. Chang, and C. Sun, "Millimeter-wave power-combining techniques," IEEE Trans. Microwave Theory Tech., vol. MTT-31, no. 2, pp. 91-107, Feb. 1983.

2. N. Camilleri, and B. Bayraktaroglu, "Monolithic millimeter-wave IMPATT oscillator and active antenna," IEEE Trans. Microwave Theory Tech., vol. 36, no. 12, pp. 1670-1676, Dec. 1988.

3. K. Chang, K.A. Hummer, and J.L. Klein, "Experiments on injection locking of active antenna elements for active phased arrays and spatial power combiners," IEEE Trans. Microwave Theory Tech., vol. 37, no. 7, pp. 1078-1084, July 1989.

4. J. Birkeland, and T. Itoh, "FET-based planar circuits for quasi-optical sources and transceivers," IEEE Trans. Microwave Theory Tech., vol. 37, no. 9, pp. 1452-1459, Sept. 1989.

5. R.N. Simons, and R.Q. Lee, "Planar dielectric resonator stabilized HEMT oscillator integrated with CPW/aperture coupled patch antenna," IEEE MTT-S Int. Microwave Symp. Dig., vol. I, pp. 433-436, 1992. (Also, NASA TM-105752, pp. 21-23, 1992.)

6. J.A. Navarro, Y.H. Shu, and K. Chang, "Wideband integrated varactor-tunable active notch antennas and power combiners," IEEE MTT-S Int. Microwave Symp. Dig., vol. III, pp. 1257-1260, 1991.

7. M. Kim, J.J. Rosenberg, R.P. Smith, R.M. Weikle, J.B. Hacker, M.P. DeLisio, and D.B. Rutledge, "A grid amplifier," IEEE Microwave Guided Wave Lett., vol. 1, no. 11, pp. 322-324, Nov. 1991.

8. R.N. Simons, and R.Q. Lee, "Nonplanar linearly tapered slot antenna with balanced microstrip feed," IEEE Antennas Propag. Soc. Int. Symp. Dig., vol. IV, pp. 2109-2112, 1992.

9. "20 GHz Monolithic Power Amplifier Module Development," NAS 3-23781.

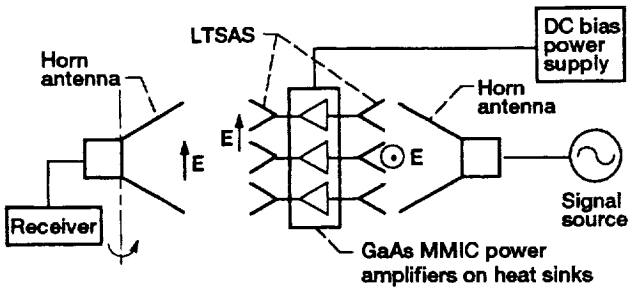

Figure 1.—Schematic illustrating a possible arrangement for space amplification.

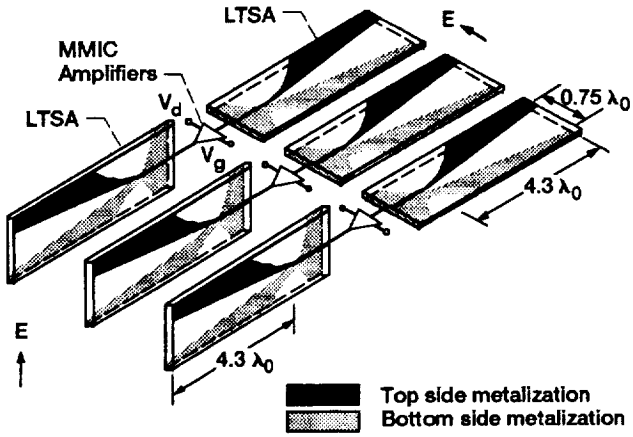

Figure 2.—Schematic illustrating the three-element array module. (λ_0: free space wavelength.)

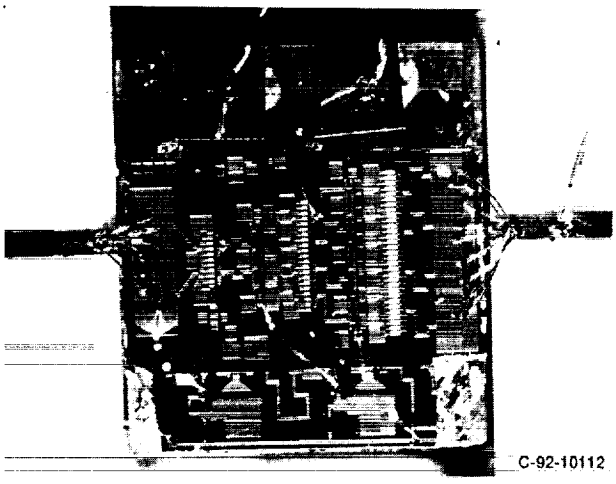

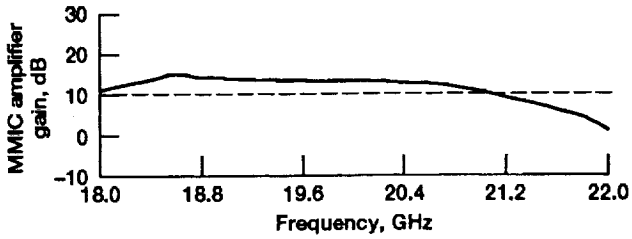

Figure 4.—Typical measured gain of MMIC amplifier.

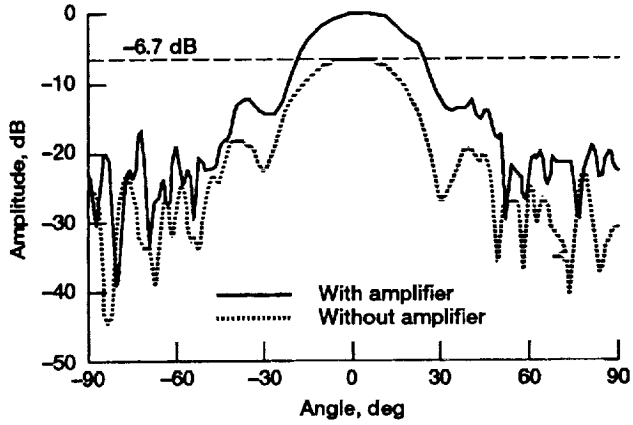

Figure 5.—The measured H-plane radiation pattern of a single LTSA with and without the amplifier.

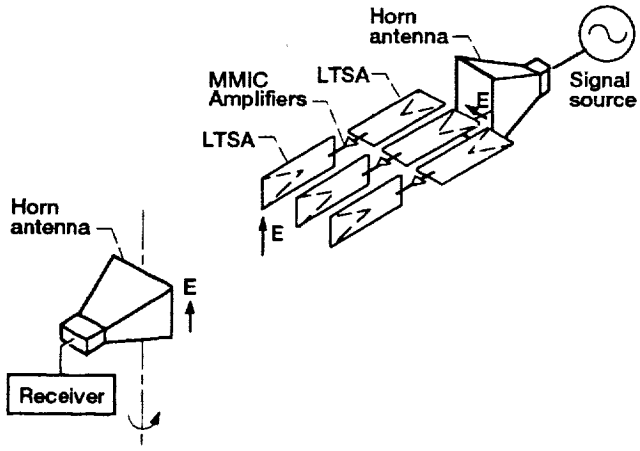

(a) H-plane.

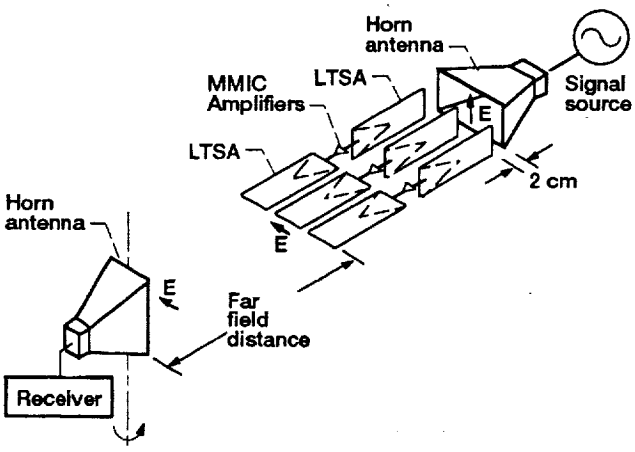

(b) E-plane.

Figure 6.—LTSA orientation in the three-element array module for gain measurement.

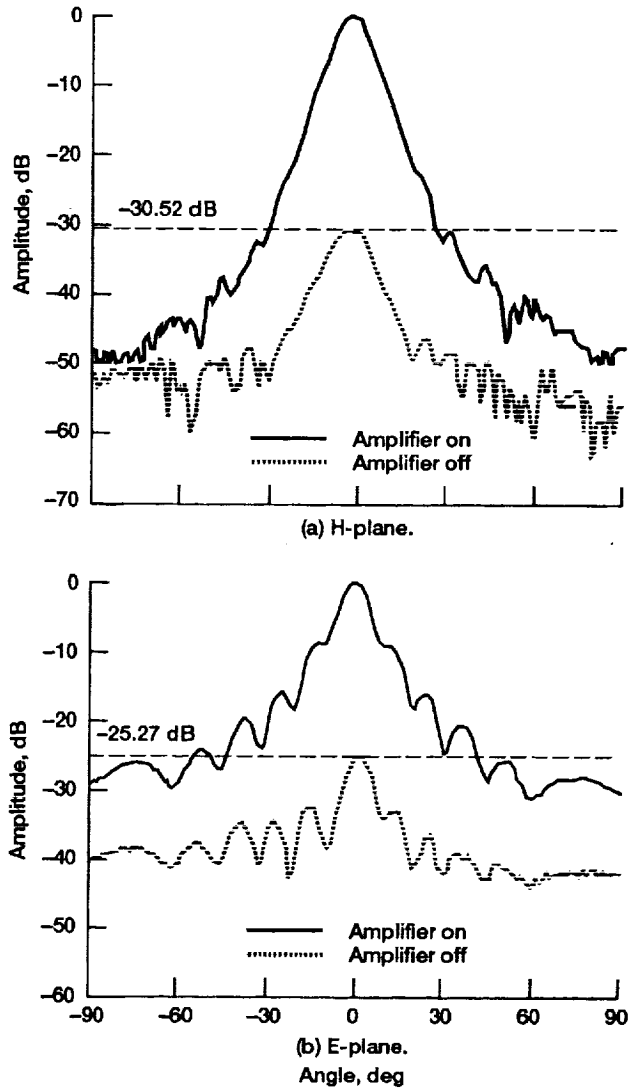

Figure 7.—The measured radiation pattern of the horn antenna showing space power amplification.

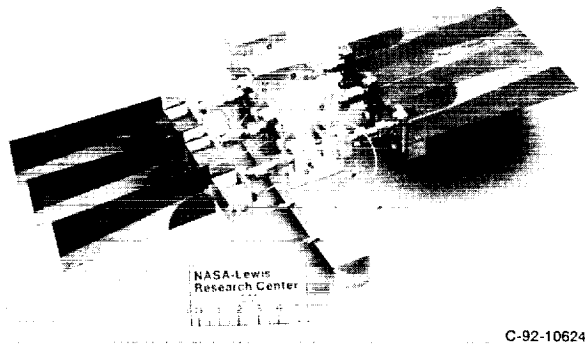

Figure 8.—The experimental three element LTSA MMIC array module.

AN ANALYSIS OF THE FREQUENCY LIMITATIONS OF AN $Al_xGa_{1-x}As/GaAs$ OPTICAL MODULATOR

M. Tabib-Azar and P. C. Claspy
Electrical Engineering and Applied Physics Department
Case Western Reserve University
Cleveland, Ohio

C. Chorey and K. B. Bhasin
National Aeronautics and Space Administration
Lewis Research Center
Cleveland, Ohio

KEY TERMS

Optical modulators, heterojunction devices, interferometers

ABSTRACT

Frequency response of an optical modulator, operating at $\lambda = 0.83$ μm and utilizing the linear electro-optic (Pockels) effect in a Mach-Zehnder configuration using an $Al_xGa_{1-x}As/Al_yGa_{1-y}As$ double heterostructure, is analyzed. We show that in semiconductor modulators, electroabsorption should be taken into account in optimizing the frequency response of the device. © *1993 John Wiley & Sons, Inc.*

I. INTRODUCTION

Light modulators, integrated with optoelectronics, have attracted intense research activities in recent years. Speed and inherent parallelism of all-optical signal processing usually justify overall larger size of the optical components, and much activity is devoted to establishing fabrication sequences that result in reliable integrated devices and waveguides [1, 2]. Electro-optic modulators based on the linear electro-optic effect are expected to have very fast response, limited only by the transit times and RCs (R is the resistance and C is the capacitance) of the geometry and, in the case of traveling-wave modulators, walk off between the light and the microwave. They are also relatively insensitive to the frequency of the light and their RCs and characteristic impedances do not change under illumination. On the other hand, the performance of electroabsorption modulators is very sensitive to the wavelength of the light and their time constants and characteristic impedances are affected by absorption. However, they can be made in much smaller sizes than the electro-optical modulators.

In most cases where one wishes to construct an electro-optic modulator from semiconductor materials, some electroabsorption cannot be avoided. This leads to slower response speeds, because the capacitance of the structure increases as electron-hole pairs (EHPs) are optically excited, as well as higher than expected attenuation. Particularly, the presence of impurity levels in the band gap can considerably contribute to the electroabsorption. In this article we analyze the performance of a $Al_xGa_{1-x}As/GaAs$ optical modulator based on the above considerations.

II. THEORETICAL CONSIDERATIONS

A typical semiconductor-based Mach-Zehnder electro-optic modulator is depicted in Figure 1(a) [2]. In this device, the integrated optical waveguide separates into two parallel branches which form the arms of the interferometer. Electrodes situated in a push-pull configuration produce the electric fields which rotate the polarization vector of the light and change its phase (the electro-optic effect) in the two arms. When the light that is traveling through these two arms is

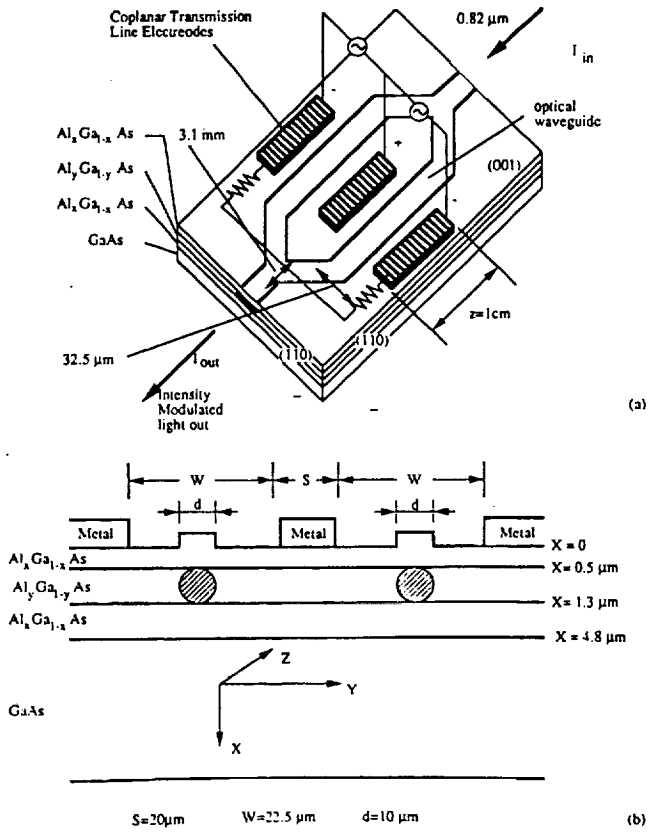

Figure 1 (a) Schematic diagram of a Mach-Zehnder modulator. (b) The cross section of the Mach-Zehnder modulator fabricated on AlGaAs/GaAs

recombined, due to mode conversion, its intensity is modulated.

A cross-sectional schematic through the parallel branches [Figure 1(b)] shows the epitaxial structure that constitutes the waveguide. It consists of three layers of $Al_xGa_{1-x}As$ grown on a semi-insulating GaAs substrate. The middle AlGaAs layer acts as the guiding channel for the light and the upper and lower layers of the AlGaAs act as cladding. The refractive indices of different AlGaAs layers are tailored by adjusting the molar ratio of the Al to Ga. The higher concentration of aluminum results in lower index of refraction. To minimize

the free-carrier absorption, all these layers are undoped. In addition, the lower layer also isolates the optical field from the GaAs substrate which has a higher refractive index than the optical channel. Two-dimensional waveguides are formed by etching ridges in the upper cladding layer, which increases the effective index of refraction in the region beneath it. The epitaxial layer thickness and ridge dimensions, shown in Figure 1(b) were chosen to produce single mode guides [3]. Figure 2(a) schematically shows ideal electro-optic modulator.

The induced phase shift in the electro-optic effect is linearly proportional to the electric field (E) and the interaction length (Z) [5]: $\Theta \propto n_0^3 r_{41} EZ$ (where n_0 is the refractive index; r_{41}, the electro-optic coefficient, for GaAs is 1.1×10^{-12} m/V). Therefore, at photon energies near the band-gap energy of the waveguide, the electro-optic effects are quite small compared to the electroabsorption which manifests itself through the exponential dependence on the absorption coefficient α: $I(z) = I_0 e^{-\alpha z}$ [where $I(z)$ is the transmitted light power at position z: I_0 is the input power]. Depending on the photon energies, α depends on the band structure (band gap), and the applied electric field (this dependence has a form of $Ee^{(-c/E)}$ as discussed later). The electroabsorption, then, with the exponential dependence on the electric field, can overwhelm the electro-optic effect. When electroabsorption occurs, the absorbed light generates electron-hole pairs (EHP). Therefore, the capacitance and the resistance of the structure changes under illumination. The change is intensity and frequency dependent.

Figure 2(b) shows the band diagram of an n-type semiconductor used in metal-insulator-semiconductor electroabsorptive modulator and Figure 2(c) after the interface. The analysis directly applies to p-type semiconductors as well. The modulating electric field, when it is positive, results in accumulation at the surface, and when it is negative, it results in depletion at the surface. The band bending is exponential in accumulation and it has square-root dependence in depletion. This yields different probabilities of light absorption, through the Franz-Keldysh effect [4], under accumulating and depleting electric fields. Also, high carrier concentration reduces the refractive index, which results in a shift in the confinement of the light. The shift is away from the interface under accumulation and it is toward the interface under depletion.

When an insulator is not used between the semiconductor and the metal electrode, accumulating electric fields result in large current conduction and cannot be used. Thus, in Schottky diode structures only depleting electric fields are used. This is a serious drawback since a depleting dc bias voltage should be applied to prevent forward conduction by a microwave. Under reverse bias, dark current flows through the diode, and depending on the heterostructure quality and the magnitude of the reverse bias, the dark current changes as a function of time, deteriorating the modulator performance.

The second problem is generation of photocurrent, which increases the power consumption of the device. The photocurrent is generated due to EHP generation and clearly it is light-intensity and frequency dependent. Any impurity levels in the band gap will contribute to the current in two ways: (i) they increase the dark current, and (ii) they modify the carrier lifetime modifying the photocurrent. The most important factor determining the response time, however, is the capacitance associated with the depletion width in the waveguide and the series resistance. The capacitance is voltage, light-intensity, and frequency dependent. As light is absorbed, the width of the depletion region becomes smaller, increasing the capacitance.

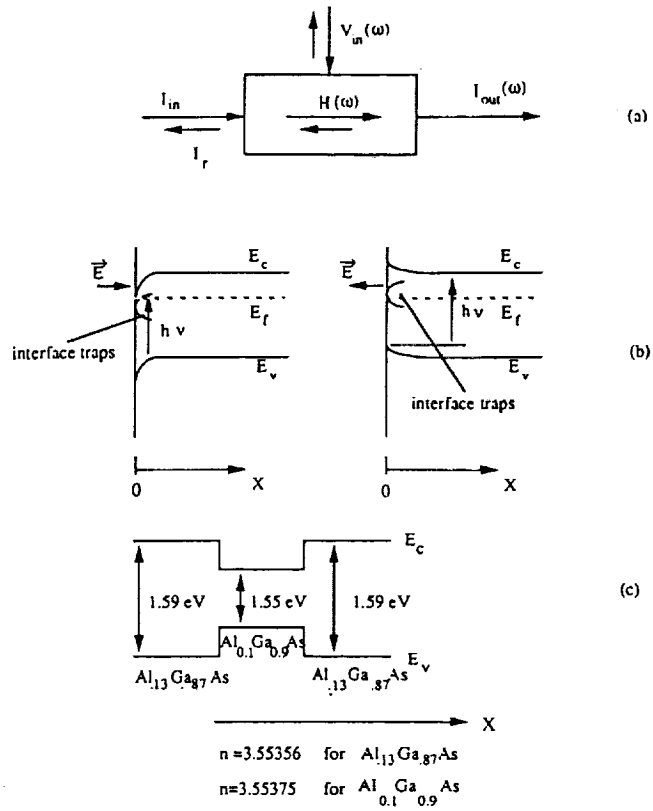

Figure 2 (a) A "black box" representation of a light modulator. (b) The band structure of a semiconductor under applied electric field. Both accumulating and depleting electric field polarities result in Franz-Keldysh effect in metal-insulator-semiconductor structures (c) The band-diagram of the modulator. The modulating electric field is applied through the high Al concentration layer at the surface

Using the above considerations, we proceed to determine the frequency characteristics of depletion capacitance of a Schottky diode when the optical generation rate and trap density are nonzero. The electric field dependence of g_{op} can be estimated as follows. First, it is easily shown that for unity quantum efficiency (i.e., one electron-hole pair per absorbed photon) the average number of EHPs generated per unit volume per second is given by $g_{op} = (1/Y)(1/Lh\nu) \int_0^L (I_0 - I)\, dx$ (where V is the volume, L is the interaction length, $h\nu$ is the photon energy, and I's are as defined before). Assuming a unit area and small α (for below band-gap illumination), it is easy to show that g_{op} is proportional to α ($g_{op} \approx \alpha \mathbf{n}/2$, $\mathbf{n}$ is the average number of electron-hole pairs generated per unit area per second). According to the Franz-Keldysh effect, the electric field dependence of the absorption coefficient is given by [5] $\alpha = (KE/\Delta E) \exp(-C(\Delta E)^{1.5}/E)$ (where K and C are

material constants and $\Delta E = E_g - h\nu$). Using the numerical values of the constants in GaAs, and for large fields ($E/4.74 \times 10^4 > 1$), we get $g_{op} \approx 1.24 \times 10^{-2}\mathbf{n}E$.

Next, using the semiconductor constitutive equations in one dimension (x) in n-type materials, and using the above g_{op}, we arrive at the following well-known linearized fourth-order partial differential equation for the potential V inside the semiconductor:

$$\partial^4 V/\partial x^4 - (1/\tau D + i\omega/D + q\mu N_D/\varepsilon_s D)\,\partial^2 V/\partial x^2 - q\mathbf{n}\alpha/2\varepsilon_s D\,\partial V/\partial x = 0. \quad (1)$$

where ρ is the charge density, ε_S is the dielectric constant of the semiconductor, n is the free carrier density, and δn is the excess carrier density. Moreover, τ is the carrier recombination lifetime, J_x is the current density, q is the elementary charge, μ is the carrier mobility, D is the diffusion constant, E_x is the electric field, and N_D is the doping concentration (all ionized: $N_D = N_{\bar{D}}$). The direction x is shown in Figure 1(b). In deriving the above equation, it is also assumed that the potential carrier density has a $e^{i\omega t}$ time dependence (ω is the radial frequency of the modulating microwave). Assuming that the position dependence of the potential is of the form $e^{\gamma x}$, γ's are given by the roots of the following algebraic equation:

$$\gamma^3 - (1/\tau D + i\omega/D + q\mu N_D/\varepsilon_s D)\gamma - q\mathbf{n}\alpha/2\varepsilon_s D = 0. \quad (2)$$

In general the potential V is given by

$$V(x) = \sum_{i=1}^{3} V_i e^{\gamma_i x} \quad (3)$$

where V_i's are determined from the boundary conditions.

The following values, which are typical in GaAs at room temperature [4], are used in solving for γ's: $\tau = 1 \times 10^{-9}$ sec, $D = 100$ cm^2/sec, $\varepsilon_s = 13 \times 8.854 \times 10^{-14}$ F/cm, $N_D = 10^{12}$ cm^{-3}, $\Delta\mathbf{E} = 20$ meV, $q = 1.6e-19$ coulomb, $k_BT/q = 0.0259$ eV (k_B is the Boltzmann constant, and T is temperature in degrees Kelvin), and $D/\mu = k_BT/q$. The values in AlGaAs, with low concentration of Al, are close to the above values, which are more exactly known in GaAs. For these values, one of the roots (γ_1) has a positive real part. Therefore, $V_1 = 0$ for V to stay bounded as x becomes large.

The ability of a modulator to properly modulate the light is closely related to the ability of an externally applied signal to modulate the potential $V(x)$ inside the semiconductor. In Figure 3, γ_2 and γ_3 as a function of frequency for different optical flux density ($\mathbf{n}$) are shown. These plots are equivalent to the plots of $\log(V_2(x))$ and $\log(V_3(x))$ as a function of $\log(f)$ curves at $x = 1$ μm. From Figure 3 it can be seen that the 3-dB point of the $\log(V_2)$ moves from 1 to 30 GHz as the $\mathbf{n}$ changes from 10^{21} photons/sec cm^2 to 10^{24} photons/sec cm^2. For values of $\mathbf{n}$ less than 10^{21} photons/sec cm^2 the change in the $\log(V_2)$ curve is negligible. Of course, this would not be the case for different values of τ and N_D.

Optical flux density of 10^{22} photons/sec cm^2 corresponds to a laser with 100-μW power operating at 1.5-eV photon energy emitting into an area of 10^6 (1000×1000) μm^2. With $\mathbf{n} = 10^{22}$ photons/sec cm^2, and the rest of the parameters as given above, γ versus $\log(f)$ plots are generated with τ as a variable as shown in Figure 4. It is interesting to note that

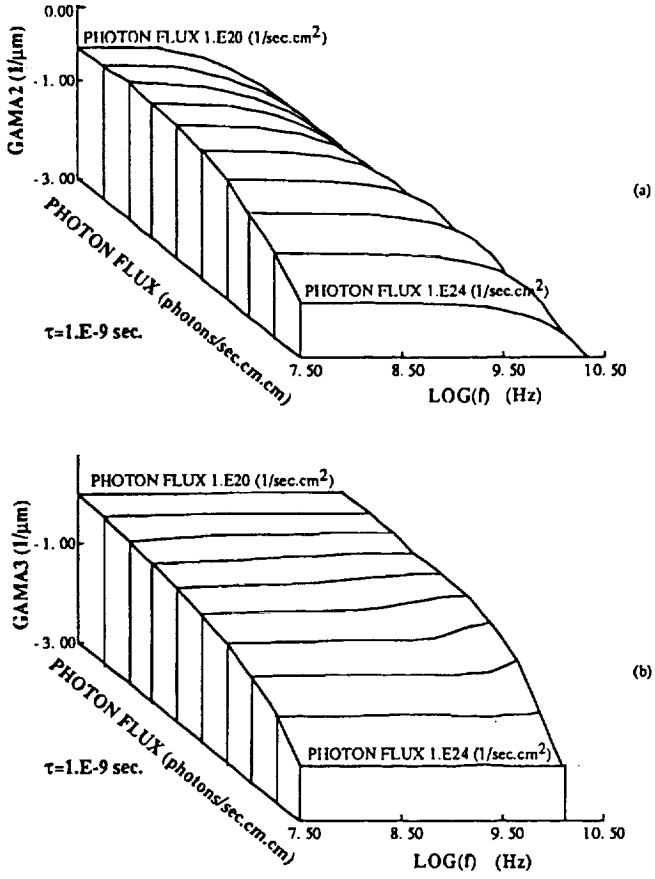

Figure 3 (a) γ_2 and γ_3 as a function of frequency and $\mathbf{n}$ (photons/sec cm^2). (b) γ_2 and γ_3 as a function of frequency and carrier lifetime τ (sec) in GaAs

shorter τ results in wider bandwidths but smaller γ_2 with γ_3 being nearly zero. Smaller γ_2 results in a potential that decays much faster inside the semiconductor. This in turn results in narrower space charge region where the gradient of the potential is not negligible.

The capacitance of the structure is approximately proportional to the inverse of the space charge width. As τ decreases or as $\mathbf{n}$ increases, the capacitance increases. If the response of the modulator is limited by the RC of the structure, larger capacitance results in larger RCs and, hence, smaller bandwidths.

III. EXPERIMENTAL RESULTS

The design and fabrication of traveling-wave Mach-Zehnder configuration electro-optic modulator, shown in Figure 1(a), has been reported elsewhere [1, 2]. Fiber optics were used to couple light in and out of the modulator. Optical coupling was accomplished by butt coupling from a single mode fiber pigtailed to a laser diode (Ortel LD-620s, peak wavelength

of 826.6 mm ~ 1.5 eV). The end facets of the modulator were prepared by cleaving; no antireflection coatings were applied. The output was monitored by an IR-sensitive camera and/or an optical power meter during alignment.

Measurements with zero applied voltage showed that the insertion loss was approximately 24 dB: this includes losses from: (1) Fresnel reflection, (2) mode mismatching between the fiber and the waveguide, and (3) absorption and scattering within the waveguide which includes losses at bends and the Y branch. The modulator 3-dB bandwidth was experimentally

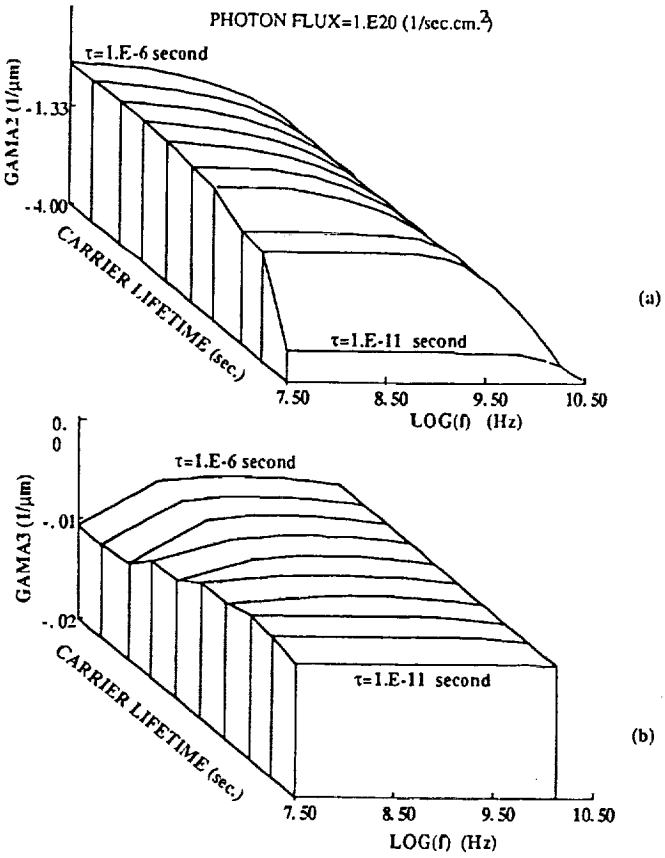

Figure 4 (a) γ_2 and γ_3 as a function of the optical flux density **n** (photons/sec cm^2). (b) γ_2 and γ_3 as a function of the carrier lifetime τ (sec) at f = 1 GHz in GaAs

measured to be 0.5 GHz [2]. The modulator was designed to have an 11-GHz bandwidth.

The observed transmitted optical intensity and the calculated $\cos^2 \phi$ intensity, expected for electro-optic modulation, as a function of applied voltage is shown in Figure 5. The observed intensity versus voltage behavior does not match the $\cos^2 \phi$ behavior, but more closely resembles a continuous exponential decrease. Observations on straight sections of waveguide (i.e., without an interferometer configuration) showed a similar decrease in intensity with applied voltage.

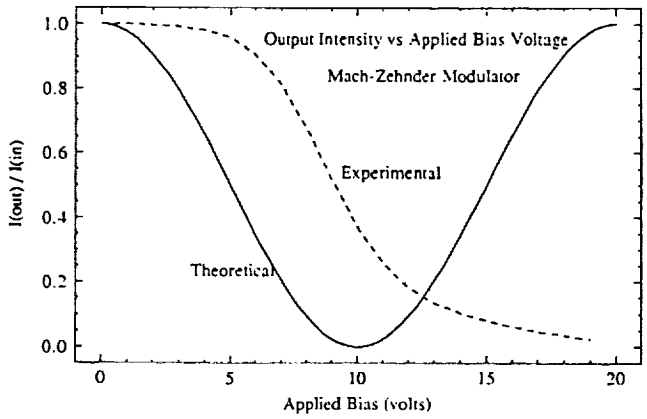

Figure 5 Theoretical output intensity versus voltage of a Mach-Zehnder modulator and the experimentally measured output intensity versus voltage

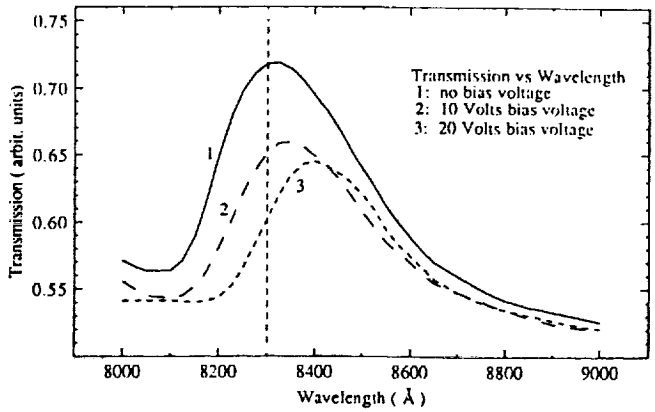

Figure 6 Experimental output intensity versus photon wavelength under different applied bias voltages

Spectroscopy was performed on the waveguides, and Figure 6 shows the observed transmission through the waveguide as a function of wavelength for applied voltages of 0, 10, and 20 V. The application of a voltage shifts the absorption edge from 814 nm (1.523 eV) at 0 V to 821 nm (1.510 eV) at 20 V, a shift of 0.013 eV. The transmission drops off at higher wavelengths partly due to waveguide cutoff and partly due to somewhat lower output of the monochromator and lower detection efficiency of the detector at larger wavelengths.

IV. DISCUSSION

According to Figure 6, the absorption edge at $V = 0$ is around 814 nm (1.52 eV). The relationship between the E_g and the composition index y when $0 < y < 0.35$ is [4] $E_g = 1.424 + 1.247y$ (eV). The 1.52-eV absorption edge means that the effective y is around 0.08 (8% Al) instead of the expected value of 0.1 (10% Al). This discrepancy can also be caused by a nonzero internal electric field when $V = 0$. From the position of the laser diode at 826 nm (1.501 eV) it is obvious that the applied voltage significantly increases the absorption. From Figures 5 and 6 it is clear that the observed intensity modulation with applied voltage is due to electroabsorption.

Any change related to the electro-optic effect is rendered unobservable by the much larger absorption effect.

To determine the bandwidth of the modulator, we note that as the light is absorbed in the $Al_yGa_{1-y}As$ layer, EHPs are generated. In the presence of an electric field, EHPs are spatially separated. Since this layer has lower Al concentration than the adjacent layers, its band gap is lower. Thus, it can contain the EHPs forming a two-dimensional low-resistivity layer. This sheet of charge provides a relatively good conducting layer. Therefore, the effective distance between the metallic electrodes is shortened and the capacitance between them is increased. Assuming that the top $Al_xGa_{1-x}As$ layer is semi-insulating, the characteristic impedance of the electrodes and the modified structure is calculated, using standard microwave programs to be 2.31 Ω. With such a large mismatch between the line impedance (50 Ω) and the modulator. With such a large mismatch between the line impedance (50 Ω) and the modulator impedance, most of the microwave power is reflected. Only at relatively low frequencies is the transmitted microwave able to modulate the potential inside the waveguide to any appreciable width. This is discussed in the previous section.

In terms of lumped parameters, the capacitance per unit area is 1.15 nf/cm^2 ($=\epsilon_s/2d$, $d = 0.5$ μm, and $\epsilon_s = 13 \times 8.854 \times 10^{-14}$), which results in an RC of 1.15×10^{-9} sec ($f \approx 0.87$ GHz). This is in good agreement with the experimentally observed bandwidth of our modulator.

V. CONCLUSION

In semiconductors the Franz-Keldysh effect, which results in an increase in optical generation rate, can increase the capacitance of the structure, lowering the bandwidth of the modulator. The effects that are discussed here can also be incorporated to increase the figure of merit, for example, by including the effect of optical generation rate, and hence the excess carrier generation on the refractive index change. This also suggests the possibility of using a second light beam to modulate light with an applied electric field as an adjustable variable that determines the coupling between the two light beams through the band bending. It can also be concluded that by incorporating an insulator (a semiconductor with a large band gap) between the metallic electrode and the channel [5, 6], the capacitance of the electroabsorptive modulator can be kept low at a reasonable value under the worst conditions.

REFERENCES

1. R. G. Walker, *J. Lightwave Technol.*, Vol. LT-5, No. 10, 1987, pp. 1444–1453.
2. C. M. Chorey, A. Ferendeci, and K. B. Bhasin, 1988 IEEE MTT-S International Microwave Symposium, New York, NY.
3. S. Y. Wang and S. H. Lin, *J. Lightwave Technol.*, Vol. 6, No. 6, 1988, p. 758.
4. S. Wang, *Fundamentals of Semiconductor Theory and Device Physics*, Prentice-Hall, Englewood Cliffs, NJ, 1989, pp. 618–620.
5. M. Tabib-Azar et al., *Proceedings of 163rd Electroch. Society Meeting*, 1983, pp. 186–190.
6. W. T. Tsang, *Appl. Phys. Lett.*, Vol. 33, 1978, p. 426.

Received 3-13-92; revised 9-28-92

SECTION TWO

SEMICONDUCTOR MATERIAL CHARACTERIZATION

Ellipsometric characterization of $In_{0.52}Al_{0.48}As$ and of modulation doped field effect transistor structures on InP substrates

S. A. Alterovitz
NASA Lewis Research Center, Cleveland, Ohio 44135

R. M. Sieg
EE Department, Cleveland State University, Cleveland, Ohio 44115

J. Pamulapati and P. K. Bhattacharya
EECS, University of Michigan, Ann Arbor, Michigan 48109

(Received 27 August 1992; accepted for publication 24 December 1992)

The dielectric function of a thick layer of $In_{0.52}Al_{0.48}As$ lattice matched to InP was measured by variable angle spectroscopic ellipsometry in the range 1.9–4.1 eV. The $In_{0.52}Al_{0.48}As$ was protected from oxidation using a thin $In_{0.53}Ga_{0.47}As$ cap that was mathematically removed for the dielectric function estimate. The $In_{0.52}Al_{0.48}As$ dielectric function was then verified by ellipsometric measurements of other $In_{0.53}Ga_{0.47}As/In_{0.52}Al_{0.48}As$ structures, including modulation doped field effect transistors (MODFET), and is shown to provide accurate structure layer thicknesses.

In this letter, we present a measurement of the dielectric function of $In_{0.52}Al_{0.48}As$ and apply it to the ellipsometric characterization of $In_{0.53}Ga_{0.47}As/In_{0.52}Al_{0.48}As$ heterostructures. The main application of $In_{0.52}Al_{0.48}As$ is as a high band gap semiconductor in $In_{0.53}Ga_{0.47}As/In_{0.52}Al_{0.48}As$ heterostructures lattice matched to InP, which are used in a variety of microwave and optical applications.[1] An important property of $In_{0.52}Al_{0.48}As$ is the fact that, unlike InP, it can be grown in thin film form by solid molecular beam epitaxy (MBE), as opposed to phosphorus containing III-V semiconductors which require gas sources. Important parameters for any applications that can be measured by ellipsometry are the thicknesses of the layers, interface quality, and surface contaminations, roughness and oxidation. In addition, the dielectric function of $In_{0.52}Al_{0.48}As$ in the visible may be useful in applications involving waveguides in this spectral range.

Ellipsometry, particularly variable-angle spectroscopic ellipsometry (VASE) in the visible and near UV, has been used to characterize, nondestructively, a variety of modulation doped field effect transistors (MODFETs)[2,3] and optoelectronic structures[4] grown on GaAs substrates. Dielectric functions of the constituents necessary for the ellipsometric analysis were taken from the literature. However, at this time no reliable experimental dielectric function of $In_{0.52}Al_{0.48}As$ has been published. Ellipsometry has been used twice in the past[5,6] to obtain the dielectric function of $In_{0.52}Al_{0.48}As$ in the visible. In Ref. 5, only results for the refractive index were published, while in Ref. 6, the dielectric function of $In_{0.52}Al_{0.48}As$ was estimated by scaling the InP values and using an effective medium model with a 3% negative voids fraction. Clearly, a direct experimental dielectric function for $In_{0.52}Al_{0.48}As$ is preferable.

In most aluminum containing III-V semiconductor ternaries, the top layer of the material will oxidize in air[7] in a time scale of hours. As ellipsometry is very sensitive to the surface conditions, we protected the top layer with $In_{0.53}Ga_{0.47}As$. We kept the thickness of this cap layer to a minimum in order to get reliable results for the $In_{0.52}Al_{0.48}As$ dielectric function in the near UV, where the light penetration depth is very small. As a check of the accuracy of our result, we used our experimental $In_{0.52}Al_{0.48}As$ dielectric function to fit two other $In_{0.53}Ga_{0.47}As/In_{0.52}Al_{0.48}As$ structures using two parameter fits only. Finally, we used our result to analyze five MBE grown $In_{0.53}Ga_{0.47}As/In_{0.52}Al_{0.48}As$ complete MODFET structures. The MODFETs were grown at two laboratories to make sure that no systematic error in the analysis was carried over from a systematic error in the growth parameters of one group.

All samples, except three MODFETs, were grown at the University of Michigan. The $In_{0.52}Al_{0.48}As$ growth temperature used was the optimum value of 520 °C that was found to result in smooth films with the least amount of clustering.[8] Some of the MODFET structures were grown at 500 °C. The growth rate was in the range 0.6–1.2 μm per hour. The ellipsometric measurements[9] were taken at 3–7 angles of incidence in the range 300–750 nm (i.e., spectral range with reasonable experimental reflectivity) with 10 nm increments. The calibration sample was measured in 5 nm increments for better resolution. Marquardt least square fits were used to estimate the desired parameters.

The calibration sample was a 1-μm-thick $In_{0.52}Al_{0.48}As$ on top of a 30 period 3 nm/3 nm $In_{0.53}Ga_{0.47}As/In_{0.52}Al_{0.48}As$ buffer. For ellipsometry purposes, the $In_{0.52}Al_{0.48}As$ was treated as the substrate, assuming it to be optically thick. The free parameters of the model were the oxide and cap layer thicknesses and the values of the $In_{0.52}Al_{0.48}As$ dielectric function at all experimental wavelengths. The calibration functions for the oxide[10] and $In_{0.53}Ga_{0.47}As$[11] were taken from the literature. The resulting $In_{0.52}Al_{0.48}As$ dielectric function ϵ is shown in Fig. 1. The values of the dielectric function for energies below 1.9 eV ($\lambda > 650$ nm) are not as accurate as those above that energy due to the light penetrating into the superlattice region. Conventionally, a layer is considered optically thick if its thickness is greater than 2δ, where δ is the light

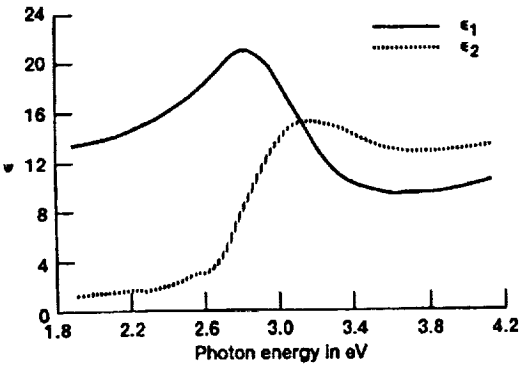

FIG. 1. Dielectric function ϵ of $In_{0.52}Al_{0.48}As$ in the range 1.9–4.1 eV. ϵ_1 and ϵ_2 are the real and imaginary parts of the dielectric function, respectively.

penetration depth.[12] We choose to be more conservative and use a 3δ cutoff criterion. The ellipsometric result also provided best fit values of 2.2 nm of oxide and 1.3 nm of $In_{0.53}Ga_{0.47}As$, which are reasonable values for a native oxide thickness and a nominal 2 nm $In_{0.53}Ga_{0.47}As$ cap. We obtained a mean square error (MSE) for the $\tan\Psi$ and $\cos\Delta$ fit[3] of 1.0×10^{-5}, where Ψ and Δ are the ellipsometric experimental results. This exceedingly low value of MSE is due to the large number of parameters.

Next, two samples of thick $In_{0.52}Al_{0.48}As$ layers were measured, both grown on InP without a superlattice buffer. Sample A had a nominal 2-μm-thick $In_{0.52}Al_{0.48}As$ while sample B had a little over a 1-μm-thick layer. Both had a thicker $In_{0.53}Ga_{0.47}As$ cap layer than the calibration sample. The ellipsometric model used for these samples included two parameters only, the thicknesses of the oxide and the $In_{0.53}Ga_{0.47}As$ cap layer. The $In_{0.52}Al_{0.48}As$ dielectric function used was the result obtained here in the first stage of the work. The results for samples A and B are summarized in Table I. The values of the MSE for these two parameter fits, especially for sample A, are extremely good. In both cases, the $In_{0.53}Ga_{0.47}As$ layer thickness estimated by ellipsometry is smaller than the nominal value. We believe some of the material was oxidized and some error may be due to the growth calibration. However, we did not encounter this discrepancy in MODFET samples made at another laboratory, as will be shown below.

The MODFET structures shown in Table II were made at both the University of Michigan (sample Nos. 1 and 2) and by a commercial vendor[13] (sample Nos. 3, 4, and 5). All structures had complex buffer layers. For example, the University of Michigan samples had the following layers: starting from the semi-insulating InP substrate, a 30 period 3 nm/3 nm $In_{0.53}Ga_{0.47}As/In_{0.52}Al_{0.48}As$ buffer layer and a 400 nm undoped $In_{0.52}Al_{0.48}As$ as the lower part of the conduction channel quantum well. The other samples (Nos. 3, 4, and 5) had additional layers below the 30 period lattice, but they had the same buffer structure just below the conduction channel. As the ellipsometric analysis was limited to the device active layers, the 400 nm $In_{0.52}Al_{0.48}As$ layer was regarded as substrate. Thus, we limited our analyses to wavelengths below 540 nm. The layer thicknesses, as estimated by RHEED, are given in Table II. In all samples, the active layers included an undoped $In_{0.53}Ga_{0.47}As$ channel, an $In_{0.52}Al_{0.48}As$ donor layer, and an $In_{0.53}Ga_{0.47}As$ cap layer. The $In_{0.52}Al_{0.48}As$ donor layer had a doped (5×10^{18} cm^{-3}, Si) 15 nm layer on top of a 5 nm undoped spacer. The cap layer was also *n* doped, at 3×10^{18} cm^{-3}, Si. In the ellipsometric model, doping effects on the dielectric function were neglected.[2,3] The nominal ellipsometric models, including all layer thicknesses for the five samples, are given in Table II under the heading "Nominal." A summary of the ellipsometric results is given in Table II under the heading "VASE." The errors shown are the 90% confidence limits obtained from the least squares fitting.[14] Representative $\tan\Psi$ and $\cos\Delta$ model fits for sample number 5 are given in Figs. 2(a) and 2(b). In general, the quality of the fits, as given by the MSE, is very good, except for sample No. 3. The results for the samples made by the commercial vendor are very illuminating. Sample Nos. 3 and 4 were grown in 1991 and were nominally equivalent, except for the cap layer thickness. The VASE results show that in both samples the $In_{0.52}Al_{0.48}As$ donor layers and the $In_{0.53}Ga_{0.47}As$ channels are much thicker than the nominal values. However, the MSE is much larger for sample No. 3, denoting a poorer

TABLE I. Best fits for layer thicknesses in nm for samples made of a thick $In_{0.52}Al_{0.48}As$ layer, considered as substrate. Analysis range 300–620 nm.

Sample	Oxide		$In_{0.53}Ga_{0.47}As$		MSE $\times10^{-4}$
	Nominal	VASE	Nominal	VASE	
A	···	2.20±0.02	20	13.3±0.1	2.7
B	···	1.3±0.1	40	32.3±0.4	5.1

TABLE II. Best fits for $In_{0.53}Ga_{0.47}As/In_{0.52}Al_{0.48}As$ MODFET layer thicknesses (in nm). Analysis wavelength range 300–405 nm. 400 nm $In_{0.52}Al_{0.48}As$ layer used as substrate.

Sample number	Oxide		$In_{0.53}Ga_{0.47}As$ Cap layer		$In_{0.52}Al_{0.48}As$ Donor layer		$In_{0.53}Ga_{0.47}As$ Channel layer		MSE$\times10^{-4}$
	Nominal	VASE	Nominal	VASE	Nominal	VASE	Nominal	VASE	
1	···	4.6±0.1	10	4.8±0.1	40	42.2±0.3	55	53.9±0.7	1.6
2	···	2.4±0.1	15	8.8±0.2	45	47.9±0.4	55	56.1±1.0	2.4
3	···	2.6±0.1	5	2.3±0.3	40	46.4±0.3	40	51.2±0.6	4.9
4	···	1.0±0.04	35	40.6±0.4	40	48.4±0.5	40	54.1±1.4	0.7
5	···	1.4±0.1	35	32.9±0.5	40	43.4±1.1	40	41.5±2.1	2.4

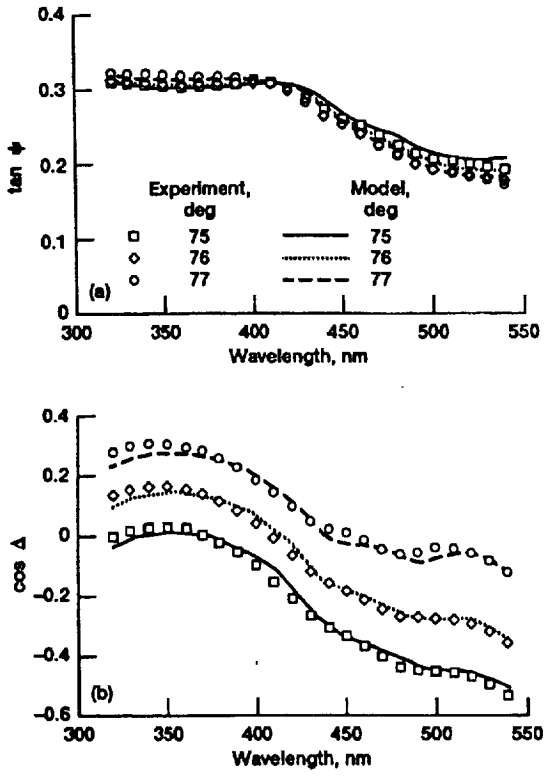

FIG. 2. Experimental and model simulation for (a) tan Ψ (b) cos Δ vs wavelength for sample number 5, Table II, for the following three angles of incidence: □ 75°, ◇ 76°, ○ 77°.

model. We speculate that the problem in this sample originates from the very thin thickness of the cap layer. The $In_{0.53}Ga_{0.47}As$ top layer may be too thin for protecting the $In_{0.52}Al_{0.48}As$ from oxidation, and the sample model shown here did not take this into account. Oxidation problems are encountered in all thin capped MODFET structures (samples No. 1, 2, and 3), where the VASE determined $In_{0.53}Ga_{0.47}As$ layer thickness is very small (see Table II). The large discrepancy between the nominal and the VASE thicknesses of the donor and channel layers in samples 3 and 4 as compared with that of sample 5 can be explained as follows. Sample No. 5 was grown 10 months after the other two samples. In the meantime, several improvements in the nominal thickness calibrations were implemented,[15] including repositioning of the RHEED gun, adjusting the shutters to reduce transients, and a better correlation between RHEED results and ternary alloy thicknesses. Indeed, for sample No. 5, the nominal and VASE thicknesses are the same to within 8% for all layers.

We also analyzed all MODFET samples using the suggested $In_{0.53}Al_{0.47}As$ dielectric function from Ref. 6. The results looked unreliable: the MSE were a factor of 5 to 18 higher for the thin $In_{0.53}Ga_{0.47}As$ capped samples; there was no consistency between sample Nos. 3 and 4; and most thicknesses were far away from the nominal values.

In summary, we have experimentally determined the dielectric function of $In_{0.52}Al_{0.48}As$ in the range 300–650 nm and have successfully applied it in the determination of the active layers' thicknesses of MODFET devices lattice matched to InP grown by MBE. This ellipsometric nondestructive characterization of high performance MODFET's that include $In_{0.52}Al_{0.48}As$ layers not only provided a confirmation of the nominal layer thickness values, but also identified problems in thickness calibrations during growth, as well as cap layer oxidation problems.

We would like to thank W. Weisbecker and L. W. Kapitan from Quantum Epitaxial Design, Inc., for making three samples and for sending private communication on their system improvements, and to D. E. Aspnes for supplying us with his $In_{0.53}Ga_{0.47}As$ results in a digital form.

[1] See, for example, *Proceedings of the Third International Conference on InP and Related Materials* (IEEE, New York, 1991).
[2] P. G. Snyder, M. C. Rost, G. H. Bu-Abbud, J. A. Woollam, and S. A. Alterovitz, J. Appl. Phys. **60**, 3293 (1986).
[3] S. A. Alterovitz, P. A. Sekula-Moise, R. M. Sieg, M. N. Drotos, and N. A. Bogner, Thin Solid Films **220**, 241 (1992).
[4] S. A. Alterovitz, J. A. Woollam, and P. G. Snyder, Solid State Technol. **31**, 99 (1988).
[5] J. Krauser, C. Borholdt, H. Kunzel, H. W. Dinges, M. Druminski, R. Gessner, and K. H. Zschauer, *Proceedings of the 4th European Conference on Integrated Optics* (SETG, Glasgow, 1987), p. 75.
[6] C. Pickering, N. S. Garawal, D. Lancefield, J. P. Piel, and R. Blunt, Appl. Surf. Sci. **50**, 346 (1990).
[7] D. E. Aspnes, S. M. Kelso, R. A. Logan, and R. Bhat, J. Appl. Phys. **60**, 754 (1986).
[8] J. E. Oh, P. K. Bhattacharya, and Y. C. Chen, J. Electron. Mater. **19**, 435 (1990).
[9] S. A. Alterovitz, R. M. Sieg, N. S. Shoemaker, and J. J. Pouch, Mater. Res. Soc. Symp. Proc. **152**, 21 (1989).
[10] D. E. Aspnes, G. P. Schwartz, G. J. Gualtieri, A. A. Studna, and B. Schwartz, J. Electrochem. Soc. **128**, 590 (1981).
[11] D. E. Aspnes and H. J. Stocker, J. Vac. Sci. Technol. **21**, 413 (1982).
[12] J. Humlicek, M. Garriga, M. I. Alonso, and M. Cardona, J. Appl. Phys. **65**, 2827 (1989).
[13] Quantum Epitaxial Design, Bethlehem, PA. 18015.
[14] D. E. Aspnes, SPIE **276**, 188 (1981).
[15] L. W. Kapitan (private communication).

Ellipsometric study of metal–organic chemically vapor deposited III–V semiconductor structures

Samuel A. Alterovitz
NASA Lewis Research Center, Cleveland, OH 44135 (USA)

Patricia A. Sekula-Moise
Spire Corporation, Bedford, MA 01730 (USA)

Robert M. Sieg*, Mark N. Drotos* and Nancy A. Bogner*
Cleveland State University, Cleveland, OH 44115 (USA)

Abstract

Metal–organic chemical vapor deposition was used to grow epitaxial layers of AlGaAs, GaAs and InGaAs on semi-insulating GaAs substrates. The ternary composition of the thick layers was determined by double-crystal X-ray diffraction (DCXRD). Variable angle spectroscopic ellipsometry was used to characterize several types of structures including relaxed single-component thick films and strained lattice multilayer structures. The thick film characterization included ternary alloy composition as determined by a numerical algorithm and interface quality. The results for the alloy composition were equal to the DCXRD results, to within the experimental errors except for the top layer of a thick AlGaAs film. The strained layer multistructures were analyzed for all layer thicknesses and alloy compositions. For most layers, the thickness was equal to the nominal values, to within the experimental errors. However, in all three $In_{0.3}Ga_{0.7}As$ samples, the indium concentration estimated from the relaxed layer's InGaAs algorithm was around 21%, *i.e.* much lower than the nominal value. This result indicates a shift in the critical points of the dielectric function, owing to strain effects.

1. Introduction

The most common technique of growing epitaxial III–V semiconductors films on III–V substrates is by molecular beam epitaxy (MBE). However, the technique of metal organic chemical vapor deposition (MOCVD) is more versatile than MBE, as it can be used to grow a larger selection of group V materials, *e.g.* phosphorus. In addition, MOCVD can produce film growth on several wafers concurrently compared with a single wafer in MBE. The materials of interest in this study are AlGaAs, InGaAs and GaAs, as they are needed to grow the multistructure needed to produce modulation-doped field effect transistors (MODFETs). This MODFET device was developed by MBE in the mid-1980s [1]. MOCVD is being used to grow strained layer InGaAs on GaAs [2, 3] but MOCVD growth of the combination of a AlGaAs layer adjacent to strained InGaAs is not common. The commercial applications of this MODFET are widespread [4], especially for materials grown on GaAs substrates. The conduction channel, made of InGaAs, is under strain. However, if the thickness of the channel is below a critical thickness h_c [5], the strained layer grows pseudomorphically on GaAs. These strain effects have essentially no effect on the electrical properties of the MODFET, but they can be important for optoelectric applications [6].

The most common technique to calibrate a MOCVD reactor for growth rate and alloy composition is to measure mechanically or by microscopy the layer thickness and to use double-crystal X-ray diffraction (DCXRD) for composition. However, DCXRD needs a relatively thick layer of material to give a reliable value of alloy concentration. A much larger thickness is needed to assume a strain-free layer and to avoid corrections to the X-ray results, as a result of strain.

In this paper we will show several ways that ellipsometry can be used to help in calibrating the MOCVD growth parameters. We will also show instances in which ellipsometry was able to pinpoint problems in the layer composition or interfaces. In addition, a quantitative measure of the strain effect on the dielectric function of $In_{0.3}Ga_{0.7}As$ will be estimated.

*Undergraduate student intern at NASA Lewis Research Center, Cleveland, OH 44135, USA.

2. Experimental details

All samples were grown by MOCVD at Spire Corporation, on semi-insulating GaAs(001) substrates, using low pressure MOCVD in an SPI-MO CVD™450 reactor. The growth temperature and pressure used for all samples were 650 °C and 53 Torr respectively. Source regeants used for these layers include trimethylgallium, trimethylindium, trimethylaluminum, and 100% arsine (AsH_3) with a palladium-diffused hydrogen carrier gas. Two sets of samples were selected for ellipsometry work: (a)thick films; (b) MODFET structures. In set a, two aluminum gallium arsenide ($Al_xGa_{1-x}As$) films were supplied from the same run (M4-2128) with an aluminum molar fraction of 18% (averaged over both samples) as measured by DCXRD. The $Al_xGa_{1-x}As$ film thickness was 8500 Å; the growth rate for this layer was 2.6 Å s^{-1}. The $Al_xGa_{1-x}As$ was protected by a thin (50 Å) GaAs cap. Two indium gallium arsenide ($In_YGa_{1-Y}As$) compositions were calibrated for Y by DCXRD. The first, M4-2093-2 has an indium concentration of 25.6% and was grown at a rate of 3.5 Å s^{-1} for a total thickness of 1.75 μm. M4-2116-2 is a 1.8 μm film of InGaAs with 30% In concentration; the growth rate for this composition was slightly higher at 4.4 Å s^{-1}. Set b contains three samples. All have the nominal structure given in Fig. 1, but with slight differences. Two of the samples have a 100 Å InGaAs channel, while one has a 50 Å channel. Also, one sample had originally a 300 Å GaAs cap layer. Some variations in the buffer among the samples were also present, but their thickness was always 1 μm with at least 9000 Å of GaAs. As ellipsometry cannot distinguish easily between doped and undoped material, we show in Fig. 1 also the initial model for ellipsometric purposes.

MODFET STRUCTURE

Nominal Structure		Nominal Structure for Ellipsometry		
		t_1	GaAs Oxide	20 Å
n GaAs	100 Å 300 Å	t_2	GaAs	100 Å 300 Å
n $Al_{0.2}Ga_{0.8}As$	400 Å			
i $Al_{0.2}Ga_{0.8}As$	50 Å	t_3	$Al_XGa_{1-X}As$	450 Å
i $In_{0.3}Ga_{0.7}As$	50 Å 100 Å	t_4	$In_YGa_{1-Y}As$	50 Å 100 Å
Buffer	10,000 Å		GaAs Substrate	
SI GaAs Substrate				

Fig. 1. Nominal structure used for ellipsometry compared with the actual nominal structure. The ternary concentrations X and Y are variables in the ellipsometric analysis.

The ellipsometric technique was described previously [7] and will only briefly be described here. In order to increase accuracy, many measurements were made using two-zone averaging [8] and/or estimating the angle of incidence by using a known sample (GaAs wafer in this case) and obtaining the correct angle by least-squares analysis. We found these corrections to be very small. A model calculation of the ellipsometric parameters $\tan \Psi_c$, $\cos \Delta_c$ was least-squares fitted to the experimental $\tan \Psi_e$, $\cos \Delta_e$, using the Marquardt algorithm to minimize the mean square error σ;

$$\sigma \equiv (N-P)^{-1} \sum_i [(\tan \Psi_{e,i} - \tan \Psi_{c,i})^2 + (\cos \Delta_{e,i} - \cos \Delta_{c,i})^2]$$

Here N is the number of experimental points and P is the number of free parameters in the model. Data at all relevant experimental angles of incidence and wavelengths are included. The dielectric functions of $Al_xGa_{1-x}As$ for any value of the aluminum concentration X were calculated using the numerical algorithm and the critical points given in ref. 10. The functions needed for $In_YGa_{1-Y}As$ for all Y values were calculated using a numerical algorithm similar to that of ref. 10, but using the following critical points (in electronvolts): from ref. 11: $E_0(Y) = 1.424 - 1.53Y + 0.45Y^2$; $E_1(Y)$ was taken as a linear approximation between GaAs and the experimental results [12] at $Y = 0.3$, $E_2(Y) = 4.8$. In this numerical calculation we found that very little difference was introduced in the dielectric functions if the E_1 critical point was exchanged with almost equal energy value of the peak in ε_1, which is much easier to deduce from the experimental result in ref. 12.

3. Results and discussion

All four thick samples were measured as received, in the wavelength range 3200–7500 Å at five angles of incidence each (around 75°). Results for the two InGaAs samples are given in Table 1. As these films were over 1.75 μm thick, we could not penetrate the thickness of the film. Thus we had only two parameters, the top oxide film thickness and the indium molar concentration Y. In Table 1 we show two results for sample M4-2093-2. In the second measurement the value of σ has improved by a factor to 2.5 because of a better angle of incidence definition obtained from measurement of a GaAs wafer.

The results for Y are basically equal to the experimental DCXRD data, to within both techniques' experimental error, indicating the reproducibility of our results compared with the sample in ref. 12 and the validity of the algorithm. The excellent values for σ

TABLE 1. Best fits for $In_yGa_{1-y}As$ thick layers, wavelength range 3200–7500 Å

	M4-2093-2		M4-2093-2		M4-2116-2	
	Nominal	Best fit	Nominal	Best fit	Nominal	Best fit
Oxide thickness	—	30.3 ± 0.6	—	27.9 ± 0.3	—	25.8 ± 0.4
In concentration (%)	25.6	24.1 ± 1.0	25.6	24.0 ± 0.5	30.0	29.9 ± 0.5
σ	—	6.4×10^{-4}	—	2.5×10^{-4}	—	7.8×10^{-4}

denote a smooth film and reliable parameter values. The results for the two AlGaAs films are given in Table 2. Here t_1(Å), t_2(Å) and t_3(Å) are the oxide, GaAs and AlGaAs thicknesses respectively and X(%) is the aluminum molar concentration. Comparison of experimental and calculated tan Ψ and cos Δ for sample M4-2128-3 before etching are shown in Fig. 2. An H_3PO_4:H_2O_2:H_2O (3:1:75) etch was performed on each sample independently. This etch can remove both GaAs and AlGaAs material. After the etch, the samples were measured in a dry nitrogen environment at an angle of incidence of 75°, with two-zone averaging. Two measurements were made on each sample, one immediately following the etch, the other 3 h later. Absolutely no change was observed as a function of the measurement delay time. Table 2 shows that, with the etch, the top oxide layer thickness increased and the AlGaAs thickness decreased as expected. We see two problems with the results in Table 2: the large values of σ compared with Table 1 and the extremely small values of GaAs thicknesses t_2 before etch. In addition, the fits given in Fig. 2 reveal very systematic discrepancies between the calculated and the experimental tan Ψ and cos Δ values in the wavelength range below 5000 Å, *i.e.* near the surface.

In order to clarify this last problem, we made fits of the data in the range 3200–5500 Å. The results are shown in Table 3. Here t_4 is the thickness of an interface layer of $Al_{0.2}Ga_{0.8}As$ with f_1(%) being the volume fraction of Al_2O_3. The very small amount of Al_2O_3 could have been formed either by the aluminum gettering action during deposition or by post-deposition oxidation from the air, through the very thin GaAs cap layer. The penetration depth of light in $Al_{0.2}Ga_{0.8}As$ in this range is always below 2000 Å. Thus, it turns out that the parameter t_3 of Table 2 cannot be estimated accurately from results in this restricted wavelength range, and therefore the $Al_xGa_{1-x}As$ was treated as a substrate. The most important result from Table 3 is that, before the etch, the top layer of the 8500 Å thick AlGaAs film does not behave like $Al_{0.2}Ga_{0.8}As$, irrespective of the interface model or the quality of fit. It seems that a long MOCVD growth of AlGaAs followed by GaAs gives a poor quality interface layer, showing up in ellipsometry by a larger aluminum concentration in the top layer than in the bulk of the film and a small amount of Al_2O_3. The etch depth of sample M4-2128-1 was about 125 Å (from Table 2), while that of sample M4-2128-3 was about 225 Å. From Table 3 we see that the X value is reduced with etching, with higher reduction for deeper etch. An approximately 225 Å etch was required to obtain the same quality AlGaAs at the top and bottom interfaces. Then, the ellipsometrically determined values of X for all wavelength range analyses are in excellent agreement with the DCXRD value. This result shows that, except for the top approximately 200 Å layer, the AlGaAs film is of good quality, with the aluminum concentration constant over all the film thickness. We have also performed best fits for the wavelength range 5600–7500 Å. In these cases we always obtained results for X and σ similar to those in Table 2. The large value of σ is probably due to inhomogeneities in the very thick AlGaAs film. This can be seen from the resonances above 6000 Å in Fig. 2, where the experimental and the calculated functions

TABLE 2. Best fits for $Al_xGa_{1-x}As$ thick films, wavelength range 3200–7500 Å

Sample	Etch	σ	t_1 (Å)	t_2 (Å)	t_3 (Å)	X (%)
M4-2128-1	Before	2.32×10^{-3}	13.8 ± 0.7	0.8 ± 2.8	8515 ± 9	20.0 ± 0.1
M4-2128-1	After	3.23×10^{-3}	32.6 ± 1.6	—	8392 ± 13	20.7 ± 0.1
M4-2128-3	Before	1.87×10^{-3}	12.2 ± 0.8	2.5 ± 2.5	8745 ± 9	19.7 ± 0.1
M4-2128-3	After	1.52×10^{-3}	23.9 ± 0.7	—	8521 ± 10	18.1 ± 0.2
Nominal values				50	8500	18

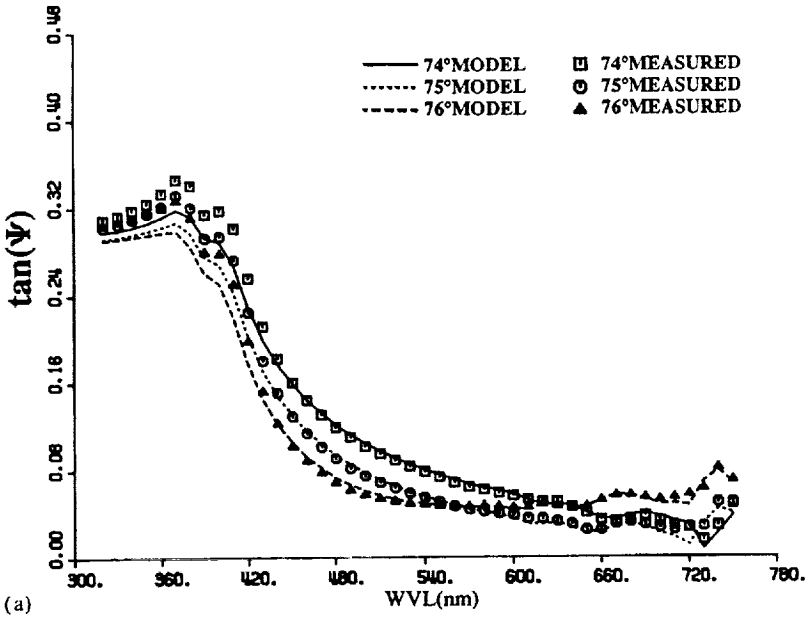

(a)

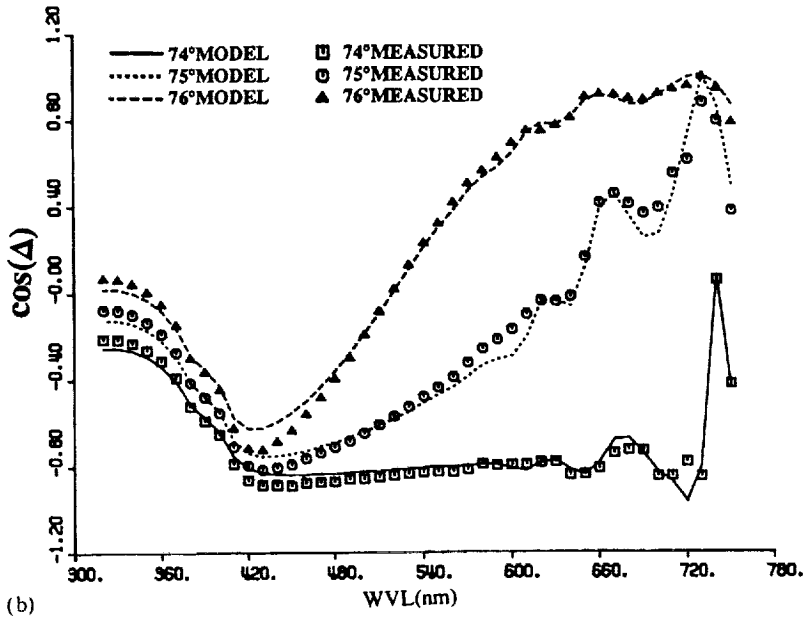

(b)

Fig. 2. Experimental and model calculated values for (a) tan Ψ and (b) cos Δ *vs.* wavelength at three angles of incidence for sample M4-2128-3 before etching.

TABLE 3. Best fits for $Al_xGa_{1-x}As$ thick films, wavelength range 3200–5500 Å

Sample	Etch	σ	t_1 (Å)	t_2 (Å)	t_4 (Å)	f_1 (%)	X (%)
M4-2128-1	Before	1.8×10^{-4}	15.8 ± 0.3	26.0 ± 1.0	—	—	28.8 ± 0.4
M4-2128-1	Before	7.3×10^{-5}	18.3 ± 0.6	13.1 ± 1.4	78 ± 7	0.8 ± 0.3	30.2 ± 0.5
M4-2128-1	After	6.6×10^{-5}	31.2 ± 0.3	—	—	—	26.2 ± 0.4
M4-2128-3	Before	2.0×10^{-4}	13.9 ± 0.3	26.3 ± 1.1	—	—	28.1 ± 0.5
M4-2128-3	Before	9.3×10^{-5}	13.6 ± 0.6	14.6 ± 1.6	75 ± 8	0.7 ± 0.4	29.5 ± 0.6
M4-2128-3	After	8.5×10^{-5}	22.1 ± 0.2	—	—	—	20.5 ± 0.3
Nominal values				50			18

have the same shape, but the magnitudes are a little different.

Results for the three MODFET structures are summarized in Table 4. Preliminary results were given in ref. 9, where no InGaAs algorithm was used. The nominal values were obtained from the prior calibration of deposition rates. The low aluminum concentrations in two of the samples are believed to be related to a possible problem in these particular runs. For all three samples, we found a correlation parameter a'_{jj} of 0.91–0.95 between the GaAs and the AlGaAs thicknesses. For the samples with the lower a'_{jj}, *i.e.* MO6-332-1 and MO6-334-1, thicknesses of all layers including both InGaAs and AlGaAs are in excellent agreement with the nominal values. For sample MO6-316-1, with $a'_{jj} = 0.95$, the value of the sum of the GaAs and AlGaAs thicknesses is within 7% of the nominal value. However, in all cases the value of Y, the indium concentration in the strained layer, is much smaller than the nominal value. For the 100 Å strained layer samples, we obtain an apparent concentration $Y = 23\%$ while for the 50 Å layer we obtain $Y = 18\%$. This result is quantitative, compared with the qualitative results obtained in ref. 9 for MBE-grown samples around $Y = 53\%$. It must be mentioned that the experimental critical thickness h_c for $In_{0.3}Ga_{0.7}As$ is around 90 Å. Thus the 100 Å InGaAs layer may be more relaxed than the thinner film, and therefore the strain effect is more pronounced for the thinner film. However, as seen from Table 4, the errors in Y make the results of all three samples overlap, around $Y = 21\%$.

In order to increase our sensitivity and to decrease the 90% confidence limits on the value of Y, we etched the thick GaAs layer of sample MO6-316-1 and remeasured it at five angles of incidence. An excellent result, with $\sigma = 8 \times 10^{-5}$, was obtained using a composite top layer, with an oxide layer thickness of 34.7 ± 3.5 Å and a 72 ± 11 Å thick layer composed of a mixture of $Al_{0.2}Ga_{0.8}As$ and $(11 \pm 4.5)\%$ of Al_2O_3. The remaining structure included the AlGaAs layer with $t_3 = 295 \pm 5.6$ Å and $X = 19.8 \pm 0.4$, and the InGaAs with $t_4 = 94.3 \pm 5.6$ Å and $Y = 21.6 \pm 0.9$. This result for Y has the lowest confidence limit. We checked the correlation of Y with the other parameters, as shown in Table 5 for sample MO6-316-1. No correlation was found, except with the InGaAs layer thickness. In all samples including the etched sample, the InGaAs thicknesses are very near to the nominal values, therefore increasing our confidence in the values of Y. Thus we believe that the value of $Y = 21\%$ for a coherently strained $In_{0.3}Ga_{0.7}As$ is reliable.

This result can be explained by changes in the critical points $E_i(Y)$, $i = 0, 1, 2$, with strain ε. Recalling the way the InGaAs algorithm was structured, we expect $E_i(\varepsilon)$ to change in an opposite way to $E_i(Y)$, *i.e.* both $E_0(\varepsilon)$ and $E_1(\varepsilon)$ to increase with ε, while E_2 will remain constant. The biaxial strain dependence of critical points in III–V semiconductors is treated theoretically

TABLE 4. Best fits for three modulation-doped field effect transistor structure samples, wavelength range 3500–6800 Å

Sample	σ	t_1 (Å)	t_2 (Å)	t_3 (Å)	X (%)	t_4 (Å)	Y (%)
MO6-316	2.4×10^{-4}	20.5 ± 0.5	337 ± 4	367 ± 6	19.7 ± 0.5	91 ± 13	24.1 ± 2.7
MO6-316	Nominal	—	300	450	20	100	30
MO6-332	5.2×10^{-4}	16.3 ± 0.5	93 ± 3	437 ± 4	14.3 ± 0.4	94 ± 6	23.5 ± 2.1
MO6-332	Nominal	—	100	450	20	100	30
MO6-334	4.7×10^{-4}	16.9 ± 0.5	99 ± 3	488 ± 5	13.7 ± 0.4	65 ± 14	18.3 ± 3.5
MO6-334	Nominal	—	100	450	20	50	30

TABLE 5. Best fits for modulation-doped field effect transistor structure sample MO6-334 using constant indium concentration values

Y (%)	σ	t_1 (Å)	t_2 (Å)	t_3 (Å)	X (%)	t_4 (Å)
10	5.19×10^{-4}	16.5 ± 0.5	99 ± 3	482 ± 5	13.3 ± 0.5	109 ± 13
15	4.74×10^{-4}	16.6 ± 0.5	99 ± 3	487 ± 5	13.4 ± 0.4	78 ± 8
17	4.68×10^{-4}	16.8 ± 0.5	99 ± 3	488 ± 5	13.6 ± 0.4	69 ± 7
18	4.66×10^{-4}	16.9 ± 0.5	99 ± 3	488 ± 5	13.6 ± 0.4	66 ± 6
19	4.66×10^{-4}	16.9 ± 0.5	99 ± 3	488 ± 5	13.7 ± 0.4	63 ± 6
20	4.67×10^{-4}	16.9 ± 0.5	99 ± 3	488 ± 5	13.7 ± 0.4	60 ± 6
22	4.70×10^{-4}	17.0 ± 0.5	99 ± 3	487 ± 5	13.7 ± 0.4	55 ± 5
25	4.74×10^{-4}	17.1 ± 0.5	100 ± 3	485 ± 5	13.8 ± 0.4	49 ± 5
30	4.88×10^{-4}	17.3 ± 0.5	100 ± 3	483 ± 5	13.9 ± 0.4	43 ± 4

in ref. 13. $E_0(\varepsilon)$ is split and both $E_0(\varepsilon)$ and $E_1(\varepsilon)$ go up with the strain. We found out, by using several values for E_0 in our algorithm, that the calculated value of the InGaAs dielectric function in our experimental range is only slightly dependent on the value of E_0 (E_0 is below 1.14 eV, for $Y > 20$). Thus, the changes in E_0 with strain can be neglected as a first approximation for small values of ε. E_1 is linear [13] for small ε, and so is the E_1 dependence on the indium concentration Y for coherently strained layers. Thus the strain dependence can be exchanged for composition dependence in our algorithm approximation. Therefore the measured 30% reduction in the value of Y with strain, together with the assumptions of linearity, gives us a simple way to measure the correct Y_c value from the measured ellipsometric result Y_e, using $Y_c = 0.7 Y_e$.

4. Conclusions

A two-prong ellipsometric study of MOCVD-grown layers of AlGaAs and InGaAs was performed, including thick films and strained layer complex structures. The study shows that the ternary composition of thick non-strained layers can be accurately determined to within experimental errors using numerical algorithms. In the case of complex structures, thicknesses of all layers and the alloy composition of non-strained layers can be determined simultaneously, provided that the correlations between parameters is no higher than 0.9. The composition of strained InGaAs can be estimated from the experimental result using a correction factor based on a linear approximation of the dependence of the critical point E_1 on composition and strain.

References

1 W. T. Masselink, A. Ketterson, J. Klem, W. Kopp and H. Morkoc, *Electron. Lett.*, *21* (1985) 937.
2 G.-W. Wang, R. Kaliski and J. B. Kuang, *IEEE Electron Device Lett.*, *11* (1990) 394.
3 W. C. Hsu, C. M. Chen and R. T. Hsu, *Appl. Phys. Lett.*, *59* (1991) 1075.
4 R. Ramanchandran and G. Metze, *Microwave J.*, *34* (1991) 113.
5 T. G. Anderson, Z. G. Chen, V. D. Kulakovskii, A. Uddin and J. T. Vallin, *Appl. Phys. Lett.*, *51* (1987) 752.
6 H. K. Choi and C. A. Wang, *Appl. Phys. Lett.*, *57* (1990) 321.
7 S. A. Alterovitz, R. M. Sieg, N. S. Shoemaker and J. J. Pouch, *Mater. Res. Soc. Symp. Proc.*, *152* (1989) 21.
8 J. M. M. de Nijs and A. van-Silfhout, *J. Opt. Soc. Am. A*, *5* (1988) 535.
9 S. A. Alterovitz, R. M. Sieg, H. D. Yao, P. G. Snyder, J. A. Woollam, J. Pamulapati, P. K. Bhattacharya and P. A. Sekula-Moise, *Thin Solid Films*, *206* (1991) 288.
10 P. G. Snyder, J. A. Woollam, S. A. Alterovitz and B. Johs, *J. Appl. Phys.*, *68* (1990) 5925.
11 Z. Hang, D. Yan, F. H. Pollack, G. D. Pettit and J. M. Woodall, *Phys. Rev. B*, *44* (1991) 10546.
12 S. A. Alterovitz, R. M. Sieg, H. D. Yao, P. G. Snyder, J. A. Woollam, J. Pamulapati, P. K. Bahattacharya and P. A. Sekula-Moise, *Proc. ICEM-90*, MRS Int. Proc., Pittsburgh, PA, 1990, p. 187.
13 F. H. Pollak, in T. P. Pearsall (ed.), *Semiconductors and Semimetals*, Vol. 32, Academic Press, Boston, MA, 1990, p. 17.

Enhancement of Shubnikov–de Haas oscillations by carrier modulation

S. E. Schacham,[a] E. J. Haugland, and S. A. Alterovitz
NASA Lewis Research Center, M/S 54-5, Cleveland, Ohio 44135

(Received 16 January 1992; accepted for publication 19 May 1992)

A drastic enhancement of the Shubnikov–de Haas (SdH) pattern is obtained by recording the *changes* in the quantum oscillations of magnetoresistance due to modulation of the carrier concentration. The technique enables measurement of the SdH waveform at relatively high temperatures and in samples with moderate mobilities. The modulated waveform shows selective enhancement of the low-frequency SdH oscillations associated with the upper subband. Thus, we were able to record very clear oscillations generated by a carrier concentration well below 5×10^{10} cm^{-2}. The theory for this selective enhancement is provided.

Several fundamental aspects concerning transport properties of carriers in a two-dimensional electron gas (2DEG) are still unresolved. As the second subband starts to be populated, does the electron concentration in the ground subband (n_1) continue to increase?[1,2] Is the mobility of electrons in the second subband larger than that at the ground level?[1–3] Does the carrier mobility drop as soon as the upper subband starts filling up[3] or even before?[4]

The primary techniques for determining most transport parameters are the Shubnikov–de Haas (SdH) oscillatory magnetoresistance, the Hall effect, and conductivity measurements. While the total carrier concentration n_T is obtained from the Hall voltage, the frequency (in $1/B$, where B is the magnetic field) of the SdH oscillation renders the electron concentration in the subbands of the 2DEG. The presence of carriers in the second subband is manifested by a superposition of the two frequencies corresponding to the concentration of electrons in the ground subband n_1 and in the upper one n_2. Most frequently $n_2<n_1$ and the determination of n_2 is extremely difficult, in particular for lower concentrations ($n_2<5\times10^{10}$ cm^{-2}).[3,5]

In this letter, we present a novel technique by which we are able to drastically enhance the SdH pattern. The technique is based on measuring the change in the magnetoresistance due to a carrier generated by a modulated light source. In addition to the overall enhancement of the SdH waveform, the technique has an important property of selectively increasing the amplitude of the slower oscillations due to carriers in the second subband much more than oscillations generated by the ground subband electrons.

The experimental setup used to generate the modulated oscillatory magnetoresistance waveform is a conventional SdH setup with an additional lock-in amplifier and a chopped laser. The sample is cooled down in an open-flow He cryostat with an optical axis to enable excitation of the carriers. The magnetic field is swept up to 1.4 T. The change in the longitudinal voltage drop is measured by a lock-in amplifier with reference frequency provided by the chopper.

Figure 1 shows the raw data obtained using the modulated SdH technique (a), followed by a regular SdH measurement (b). Both measurements were taken at 4.2 K on an InGaAs/AlGaAs high electron mobility transistor (HEMT) structure with a 200 Å $In_{0.1}Ga_{0.9}As$ well, a 100-Å-wide $Al_{0.15}Ga_{0.85}As$ spacer, and a 2×10^{18} cm^{-3} Si-doped barrier of the same composition. The identical frequency of oscillation of 12.4 T seen in Figs. 1(a) and 1(b) indicates a carrier concentration of 6.01×10^{11} cm^{-2} in the 2DEG. The *raw* modulated waveform is as good as the best computed SdH pattern derived after background subtraction and normalization. The experimentally modulated results are superior to those obtained by taking the numerical

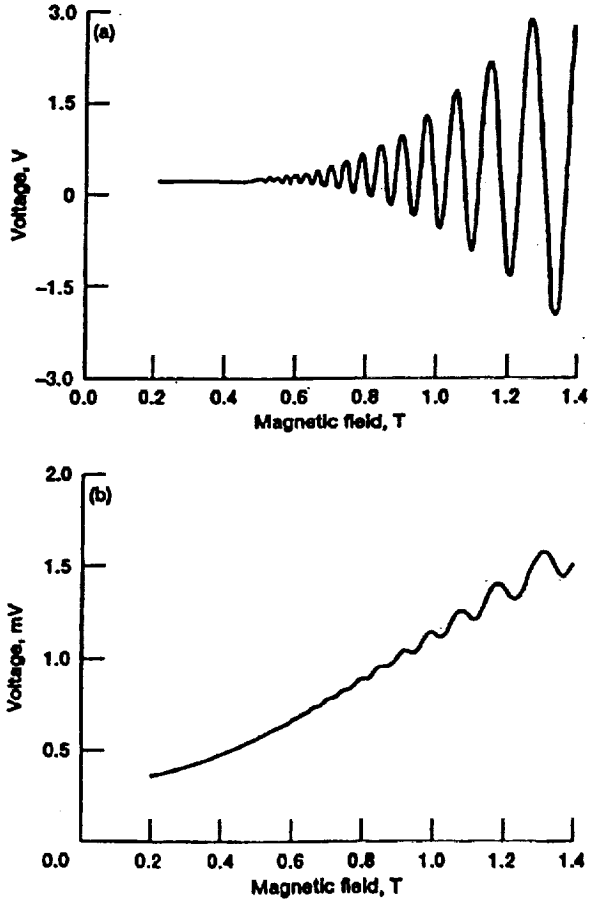

FIG. 1. SdH oscillations at 4.2 K on an $In_{0.1}Ga_{0.9}As/Al_{0.15}Ga_{0.85}As$ HEMT structure with $n=6.01\times10^{11}$ cm^{-2} and $\mu_e=97\,000$ cm^2/V s. (a) Raw modulated data. (b) Regular SdH.

[a]National Research Council–NASA Senior Research Associate, on leave from the Dept. of Electrical Engineering and Solid State Institute, Technion–Israel Institute of Technology, Haifa 32000, Israel.

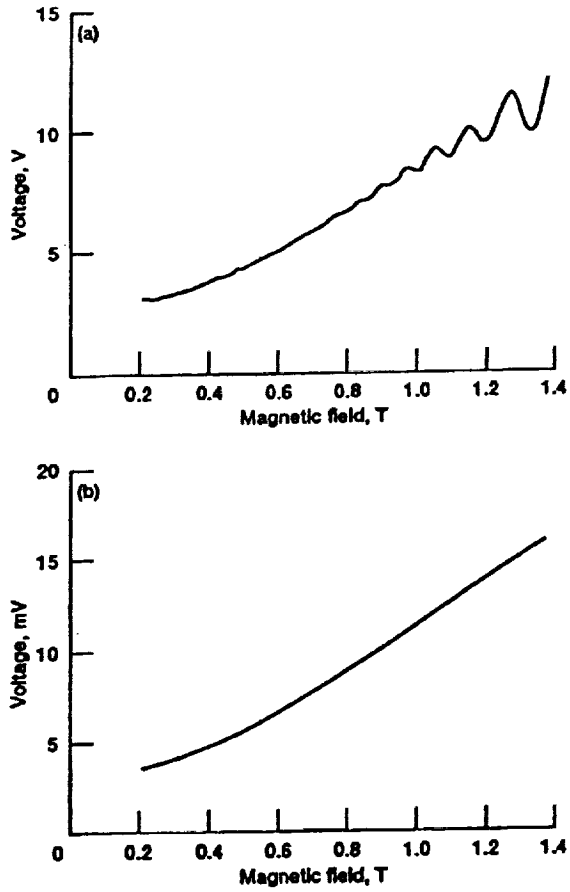

FIG. 2. Same as Fig. 1, taken at 9.1 K.

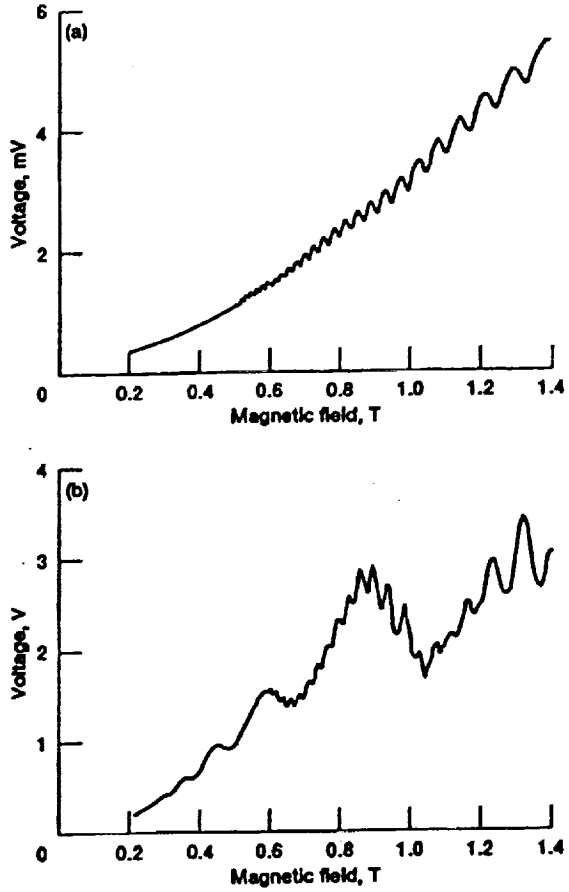

FIG. 3. SdH oscillations at 1.95 K on an $Al_{0.3}Ga_{0.7}As/GaAs$ HEMT structure. (a) Regular SdH. (b) Raw modulated data. Note the clear low-frequency oscillations.

derivative with respect to the magnetic field,[6] as will be discussed below. Figure 2 shows SdH waveforms for the same sample measured at 9.1 K. The enhancement of the waveform by the carrier modulation technique is obvious. The oscillations obtained with this carrier modulation method are very clear at this relatively high temperature, even though the electron mobility is not too large (μ_e $=97\,000$ cm^2/V s at 4.2 K).

The technique has an important property of selectively increasing the amplitude of the slower oscillations due to carriers in the upper subband much more than oscillations generated by the ground subband electrons. This selective enhancement is demonstrated in Fig. 3 on an $Al_{0.3}Ga_{0.7}As/GaAs$ HEMT structure grown on semi-insulating GaAs. The undoped AlGaAs spacer is 60 Å and the dopant concentration is 3×10^{18} cm^{-3}. The measurements are taken at 1.95 K. Figure 3(a) shows the raw data for a regular SdH measurement, from which the modulation at the lower frequency can be extracted only after background subtraction. The raw data for modulated SdH is shown in Fig. 3(b). The amplitude of oscillation at the lower frequency is significantly larger than that generated by the ground subband. The Fourier transform of the modulated SdH shows a very clear peak at a frequency corresponding to a second subband concentration of 8.4×10^{10} cm^{-2} as compared to 9.7×10^{11} cm^{-2} for the ground one. The Hall concentration n_T is 1.06×10^{12} cm^{-2} and the Hall mobility is μ_e $=410\,000$ cm^2/V s.

The selective enhancement can be caused either by an uneven distribution of the carriers between the two subbands, or by the different effect of the excess carriers on the amplitudes of oscillation. The ratio between the oscillatory resistance ΔR_{xx} and its zero-field value R_0 for a two subband system is given by[1]

$$\frac{\Delta R_{xx}}{R_0}=A_1\frac{\Delta g_1}{g_0}+A_2\frac{\Delta g_2}{g_0}+B_{12}\frac{\Delta g_1\Delta g_2}{g_0^2}, \tag{1}$$

where A_1 and A_2 are the amplitudes of oscillations at either frequency while B_{12} represents the intermodulation term. The zero-field density of states is g_0, while is oscillatory parts are given by

$$\Delta g_i=2g_0\sum_s D_T(sX)\exp\left(\frac{-s\pi}{\omega_c\tau_{q_i}}\right)\cos\left(\frac{h\pi n_i}{qB}+s\pi\right), \tag{2}$$

where $D_T(Y)=Y/\sinh(Y)$, $X=2\pi^2kT/\hbar\omega_c$, T is the temperature, ω_c the cyclotron frequency, τ_{q_i} the quantum re-

laxation time, and $i=1,2$ denotes the subband. Practically the first Fourier component $s=1$ suffices to describe most oscillations.[7]

The modulation of the carrier concentration results in a change in the oscillatory resistance $\delta(\Delta R_{xx})$ given by

$$\delta\left(\frac{\Delta R_{xx}}{R_0}\right)=\left[\left(\frac{\partial A_1}{\partial n_1}+\frac{\partial B_{12}}{\partial n_1}\frac{\Delta g_2}{g_0}\right)\frac{\Delta g_1}{g_0}+\left(\frac{A_1}{g_0}+B_{12}\frac{\Delta g_2}{g_0^2}\right)\frac{\partial \Delta g_1}{\partial n_1}\right]\delta n_1+\left[\left(\frac{\partial A_2}{\partial n_2}+\frac{\partial B_{12}}{\partial n_2}\frac{\Delta g_1}{g_0}\right)\frac{\Delta g_2}{g_0}+\left(\frac{A_2}{g_0}+B_{12}\frac{\Delta g_1}{g_0^2}\right)\frac{\partial \Delta g_2}{\partial n_2}\right]\delta n_2, \tag{3}$$

where the excess concentration δn_T is divided between the two subbands as δn_1 and δn_2. A straightforward interpretation for the enhancement of oscillations due to the upper subband would be that the electron concentration at the ground subband remains almost unchanged once the second subband starts getting populated,[2] and therefore, $\delta n_2 \gg \delta n_1$. However, most reported data indicate that the electron concentration in the ground subband continues to increase, as were our measurements on the samples described above. Moreover, it is reported that δn_1 is larger than δn_2.[8] Therefore, this cannot be the cause of the selective enhancement.

Next, the derivative terms in Eq. (3) are investigated. The derivative of the density of state is given by

$$\frac{\partial \Delta g_i}{\partial n_i}=2g_0 D_T(X)\exp\left(-\frac{\pi}{\omega_c\tau_{q_i}}\right)\times\left[\frac{\pi}{\omega_c\tau_{q_i}^2}\frac{\partial \tau_{q_i}}{\partial n_i}\cos\left(\frac{h\pi n_i}{qB}+\pi\right)+\frac{h\pi}{qB}\sin\left(\frac{h\pi n_i}{qB}\right)\right]. \tag{4}$$

This result obtained for carrier modulation should be compared with the technique of differentiating with respect to the magnetic field.[6] Taking the derivative with respect to B results in a multiplication by n_i, and since $n_1 \gg n_2$, that technique greatly enhances the signal due to the *ground* subband. It should be emphasized that the carrier modulation technique provides experimentally a derivative with respect to n. Since $\omega_c=qB/m^*$, both terms in the square brackets in Eq. (4) are multiplied $1/B$. Thus, there is a relative increase in the amplitudes at low fields. The first term depends on the change in quantum relaxation time with subband population. Little data is available on this dependence. A theoretical analysis is provided by Isihara and Smrcka,[9] from which one can derive that

$$\tau_q \propto \left|\frac{\epsilon_F}{\epsilon_F^2+[\epsilon_\sigma-3(\epsilon_\tau^2/\epsilon_\sigma)]\epsilon_F+\epsilon_\tau^2}\right|^2, \tag{5}$$

where ϵ_F is the Fermi energy and ϵ_τ and ϵ_σ are the energies at which the relaxation time and the conductivity reach their maximum. Since the electron concentration depends linearly on the Fermi level, Eq. (5) can be transformed to a dependence on n. Thus, τ_q increases steeply with increasing population at low values of n since at low energies the states become localized and resonant scattering dominates. It reaches a maximum at a concentration corresponding to ϵ_τ, and dropping from there on as the electrons can get closer to the scattering impurities.[10] Therefore, the contribution of this derivative term is much larger for the upper subband, with its low concentration. The quantum lifetime of electrons in the ground subband may have reached its peak, i.e., the derivative is close to zero. Thus, the contribution of this term to the oscillations waveform is much larger for the second subband.

The last part to be analyzed is the derivatives of the amplitudes of oscillations and the intermodulation. Expressions for the amplitudes were derived by Coleridge[1] based on the effect of various scattering mechanisms on the relaxation time. It can be shown for the case of $n_1 \gg n_2$ that

$$A_1 \simeq 2-\frac{P_{12}}{P_{11}+P_{12}};\quad A_2 \simeq B_{12} \simeq \frac{P_{12}}{P_{11}+P_{12}}, \tag{6}$$

where P_{11} is the intraground subband scattering probability and P_{12} is the intersubband scattering probability. It is clear from the equation that if A_2 increases, A_1 decreases and vice versa. Following the drop of mobility at the onset of population of the second subband, the mobility increases with increasing carrier population. Since the dominant scattering mechanism is due to the ionized impurities, this scattering is reduced by additional carriers screening this potential. Thus, it can be deduced that the intrasubband scattering decreases with increased carrier concentration. Reviewing Eqs. (3) and (6), one can expect a positive contribution to the modulated signal generated by carriers in the upper subband due to the positive derivative of A_2, but a negative contribution to the modulated amplitude by excess carriers in the ground subband since the derivative of A_1 is negative. The derivatives of the intermodulation are both positive, but as long as the oscillations are not very large (as is usually the case when the modulated SdH technique is used), this term, proportional to the square of the oscillations, is negligible.

[1] P. T. Coleridge, Semicond. Sci. Technol. 5, 961 (1990).
[2] H. L. Stormer, A. C. Gossard, and W. Wiegmann, Solid State Commun. 41, 707 (1982).
[3] J. J. Harris, D. E. Lacklison, C. T. Foxon, F. M. Stelten, A. M. Suckling, R. J. Nicholas, and K. W. J. Barnham, Semicond. Sci. Technol. 2, 783 (1987).
[4] R. Fletcher, E. Zaremba, M. d'Iorio, C. T. Foxon, and J. J. Harris, Phys. Rev. B 41, 10 649 (1990).
[5] R. J. Nicholas, M. A. Brummel, and J. C. Portal, J. Cryst. Growth 68, 356 (1984).
[6] D. R. Leadley, R. J. Nicholas, J. J. Harris, and C. T. Foxon, Semicond. Sci. Technol. 4, 885 (1989).
[7] P. T. Coleridge, R. Stoner, and R. Fletcher, Phys. Rev. B 39, 1120 (1989).
[8] D. Delagebeaudeuf and N. T. Linh, IEEE Trans. Electron Devices ED-29, 955 (1982).
[9] A. Isihara and L. Smrcka, J. Phys. C 19, 6777 (1986).
[10] See Fig. 3 of Ref. 14.

TEMPERATURE INDEPENDENT QUANTUM WELL FET WITH DELTA CHANNEL DOPING

P. G. Young, R. A. Mena, S. A. Alterovitz, S. E. Schacham, and E. J. Haugland

Indexing terms: Field-effect transistors, Transistors, Semiconductor devices and materials

A temperature independent device is presented which uses a quantum well structure and delta doping within the channel. The device requires a high delta doping concentration within the channel to achieve a constant Hall mobility and carrier concentration across the temperature range 300–1·4 K. Transistors were RF tested using on-wafer probing and a constant G_{max} and F_{max} were measured over the temperature range 300–70 K.

Introduction: In most semiconductor devices, the gain changes as a function of temperature. For a high electron mobility transistor (HEMT), as the temperature is lowered, the gain is enhanced due to lower electron scattering while maintaining an acceptable carrier concentration. When designing circuits and devices for applications requiring operation over a large temperature range, this enhancement of the carrier mobility has to be taken into account. Previous studies on delta doped channel structures [1–4] have shown that the delta doping creates band bending within the channel allowing for the quantisation of the carrier states within the doped region.

We propose a temperature independent FET with a heavily delta doped GaAs quantum well channel using molecular beam epitaxy (MBE). In the channel doped structure, temperature independence is achieved via proper ion sheet densities within the channel region that degrades the peak mobility of the carrier but creates a constant mobility and carrier concentration from 300 to 1·4 K. This doping technique is contrary to typical HEMT devices where the doping occurs outside the channel in order to reduce ion scattering at low temperatures.

Device structures and characterisation: The nominal structures grown by MBE for this work are shown in Fig. 1. The conduction channel is a GaAs layer of 150 Å confined between two $Al_{0.3}Ga_{0.7}As$ layers to form a quantum well. The channel layer is delta doped in the centre with silicon to nominal concentrations of $1{\cdot}8 \times 10^{12}/cm^2$ or $6 \times 10^{12}/cm^2$. The different dopant concentrations were used to determine the effect of the dopant concentration level on the parametric temperature dependance. The quantum well structure is used to reduce parallel conduction and improve the output conductance of the resulting device.

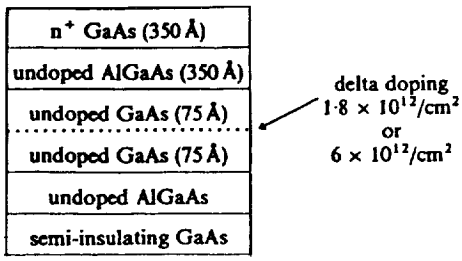

Fig. 1 *Device structure cross-section*

Fabrication of transistors and Hall bar structures was carried out using wet mesa isolation techniques. The transistors are a dual, Ti/Au gate design with gate lengths and width of 0·8–1·2 μm and 200 μm, respectively. Ohmic contacts consist of sequentially evaporated Au/Ge/Au/Ni/Au metal.

Testing of the devices was carried out to determine material transport parameters and transistor performance. The transport properties of the structures were measured by Hall and Shubnikov-de Haas (SdH) techniques over a temperature range 300–1·4 K with a maximum magnetic field of 1·4 T and carrier light modulation capability. Transistors were RF tested using an HP8510 ANA and an in-house fabricated cryostat mounted with Design Techniques probes capable of on-wafer probing of the device *S* parameters down to 65 K.

Results and discussion: Fig. 2*a* and *b* show the measured Hall mobility and carrier concentrations for the two devices as a

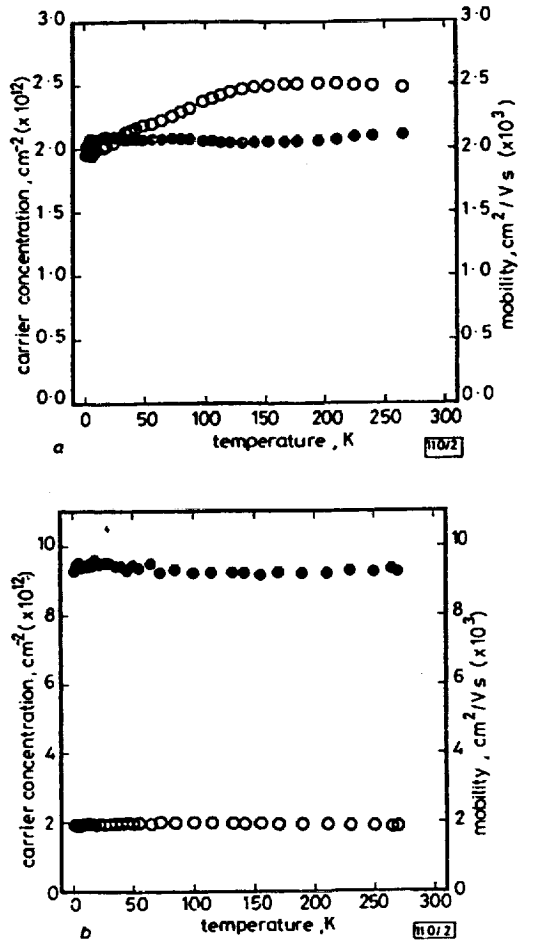

Fig. 2 *Hall mobility and carrier concentration against temperature*
- O mobility
- ● carrier concentration

a Nominal silicon doping $2 \times 10^{12}/cm^2$
b Nominal silicon doping $6 \times 10^{12}/cm^2$

function of temperature. As can be seen, the Hall mobility for the lower doped structure varied by 27% over the temperature range with maximum a Hall mobility of 2500 cm^2/Vs. The temperature dependence below 125 K is consistent with scattering from ionised impurities. The carrier concentration variation of only 5% is considered to be temperature independent and indicates there is no carrier freeze out.

When the delta doping concentration is increased by a factor 3·3 to a nominal level of $6 \times 10^{12}/cm^2$, the structure experiences a fluctuation of the electron mobility of only 7% over the same temperature range but at the expense of the magnitude of Hall mobility. The Hall mobility was measured to be $\sim 2000\,cm^2/Vs$ which is a 20% decrease over that of the lower doped sample at room temperature. The carrier concentration also showed a small 5% variation over the temperature range. Thus a stable carrier concentration is obtained over the temperature range for both dopant levels but only the higher doped sample experiences constant Hall mobility.

Finally, very high 2-D carrier concentrations were observed in these structures. For the lower doped sample, a dark Hall electron concentration of $2{\cdot}1 \times 10^{12}/cm^2$ was measured as compared to a value of $2{\cdot}7 \times 10^{12}/cm^2$ under illumination. The large photoconductivity (PC) effect leads to an enhanced signal of the SdH oscillation enabling quantitative measurements and positively confirm the 2-D character of the carriers. Quantitatively, we found carrier concentrations under illumination for the ground and first excited sub-bands of $2{\cdot}1 \times 10^{12}/cm^2$ and $5{\cdot}3 \times 10^{11}/cm^2$, respectively. This shows that for the low doped sample, only two sub-bands are populated. We could not resolve all the sub-bands by SdH for the higher doped sample, but we expect more sub-bands to be populated. This larger number of populated sub-bands is the main reason for temperature independent mobility, as the electrons in the higher sub-bands are spatially less affected by the ionised impurity scattering [5].

To demonstrate the temperature independence of the structure, FETs made from the highly doped structures were tested from 70 to 300 K. The S parameters were measured on-wafer to determine F_{max} and G_{max} at 5 GHz as a function of temperature. G_{max} and F_{max} are shown in Fig. 3. An average G_{max} of 7·3 dB was measured over the whole temperature range at 5 GHz with a variation of only $\pm 0{\cdot}35$ dB. The devices were

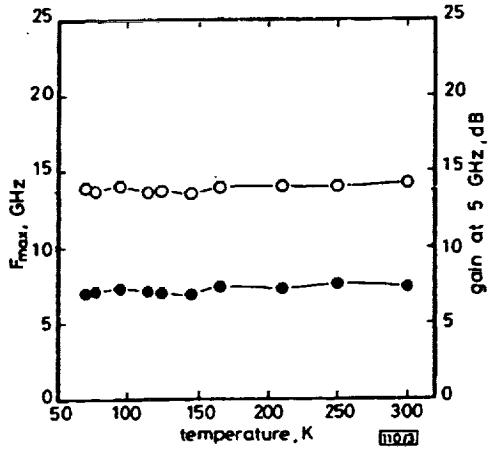

Fig. 3 *G_{max} and F_{max} against temperature for 1 μm device*
○ F_{max}
● G_{max}

stable across the frequency range and this constant stability appears to be characteristic of the structures with channel delta doping. Results for F_{max} show a similar effect with F_{max} being only affected by system noise and not dependent on temperature.

Conclusion: A device quantum well structure with channel doping has been demonstrated with temperature independent parameters. Electron Hall mobility and carrier concentration were almost constant against temperature independence of the RF performance for the transistors. With G_{max} and F_{max} remaining unchanged over the whole temperature range, the need for temperature compensation is eliminated and cryogenic design of circuits using the room temperature S-parameters is viable.

26th May 1992

P. G. Young*, R. A. Mena, S. A. Alterovitz, S. E. Schacham† and E. J. Haugland (*NASA Lewis Research Center Cleveland, Ohio 44135, USA*)

* Permanent address: Department of Electrical Engineering, University of Toledo, Toledo, Ohio 43606, USA
† Permanent address: Department of Electrical Engineering, Technion-Israel Institute of Technology, Haifa 32000, Israel

References

1 HONG, W., HARRISON, J., FLOREZ, L., and ABELES, J.: 'DC and AC characteristics of Delta-Doped GaAs FET', *IEEE Electron Device Lett.*, 1989, 19, pp. 310–311
2 SHUBERT, E., CUNNINGHAM, J., and TSANG, W.: 'Self-aligned enhancement-mode and depletion mode GaAs field-effect transistors employing the delta doping technique', *Appl. Phys. Lett.*, 1986, 49, pp. 1729–1731
3 MAKIMOTO, T., KOBAYASHI, N., and HORIKOSHI, Y.: 'Electron conduction in GaAs atomic layer doped with Si', *J. Appl. Phys.*, 1988, 63, pp. 5023–5026
4 ZRENNER, A., REISINGER, N., and KOCH, F.: 'Electron subband structure of a δ(z)-doped layer in n-GaAs'. 17th Int. Conf. on Phys. of Semiconductors, 1984, San Francisco, CA, August, pp. 325–328
5 SHUBERT, E., CUNNINGHAM, J., and TSANG, W.: 'Electron-mobility enhancement and electron-concentration enhancement in delta-doped n-GaAs at T = 300 K', *Solid State Commun.*, 1987, 63, pp. 591–594

Room-temperature determination of two-dimensional electron gas concentration and mobility in heterostructures

S. E. Schacham,[a] R. A. Mena, E. J. Haugland, and S. A. Alterovitz
National Aeronautics and Space Administration, Lewis Research Center, Cleveland, Ohio 44135

(Received 30 September 1992; accepted for publication 11 January 1993)

A technique for determination of room-temperature two-dimensional electron gas (2DEG) concentration and mobility in heterostructures is presented. Using simultaneous fits of the longitudinal and transverse voltages as a function of applied magnetic field, we were able to separate the parameters associated with the 2DEG from those of the parallel layer. Comparison with the Shubnikov–de Haas data derived from measurements at liquid helium temperatures proves that the analysis of the room-temperature data provides an excellent estimate of the 2DEG concentration. In addition we were able to obtain for the first time the room-temperature mobility of the 2DEG, an important parameter to device application. Both results are significantly different from those derived from conventional Hall analysis.

Two of the most important physical parameters governing the performance of devices based on two-dimensional electron gas (2DEG) are the concentration of carriers forming the 2DEG and their mobility. In the past, the main effort was placed on increasing the carrier mobility by separating the doped layer from the conduction channel. This was realized using either homogeneous or planar doping in the barrier while the conduction took place in the channel, i.e., a modulation doped (MOD) structure. Lately the trend is to obtain as high a 2DEG concentration as possible. Dopants are introduced into the channel,[1,2] drastically reducing the carrier mobility, defeating the concept of a MOD structure. There is a tradeoff between increased doping level and mobility of the carriers in the channel. In all cases, the determination of the 2DEG concentration and mobility is an essential part of the characterization of high speed devices.

Unfortunately the determination of the concentration and mobility of carriers is frequently complicated by the presence of a parallel conducting path, in most cases in the barrier layer, since it is usually heavily doped. Typical room-temperature concentrations in the parallel conduction path, AlGaAs for GaAs based devices, and InAlAs for InP based devices, are of the order of 10^{18} cm^{-3}. Even though the mobility of these carriers is substantially smaller than that of carriers in the 2DEG, in particular in MOD structures, their presence may significantly modify the Hall coefficient R_H and conductivity data.[3] Thus, it becomes essential to resort to measurements performed at cryogenic temperatures, in order to determine the 2DEG concentration, assuming it remains constant as a function of temperature.

In this letter we propose a technique that enables the determination of the 2DEG concentration using only room-temperature measurements. At the same time the room-temperature 2DEG mobility is derived, which is a parameter of utmost importance in development of high speed devices. The technique is based on recording of both the longitudinal and transverse (Hall) voltages across the sample versus magnetic field, determining the physical magnetoresistance and the change in the Hall voltage as a function of field.

The general expressions for the longitudinal and transverse resistivities as a function of magnetic field B (in the z direction) in the presence of two carriers are given by:[3]

$$\rho_{xx}=E_x/J_x=D_{12}/(D_{12}^2+A_{12}^2), \tag{1}$$

$$\rho_{yx}=E_y/J_x=R_H B=-A_{12}/(D_{12}^2+A_{12}^2), \tag{2}$$

with

$$D_i=n_i e^2\tau_i/m_i(1+\omega_{ci}^2\tau_i^2)$$

$$A_i=\omega_{ci}\tau_i D_i$$

$$D_{12}=D_1+D_2$$

$$A_{12}=A_1+A_2.$$

In this letter we assume that the carriers in the conduction channel of the heterostructure form a 2DEG and we will denote these carriers with index 1 and those in the parallel path with index 2. The concentrations of the two carriers are n_i, their effective masses are m_i and the scattering times are τ_i, with $i=1,2$ for the two carriers. E is the electric field while the longitudinal current density is denoted by J_x (see insert in Fig. 1). The Hall concentration and mobility will be denoted by n_H and μ_H and the Hall scattering factor is assumed to be equal to 1. The magnetic field dependence is introduced through the cyclotron frequency, $\omega_{ci}=eB/m_i$, where e is the electron charge. At zero magnetic field the longitudinal resistivity is equal to the parallel combination of the resistivities of the two carriers, while at very large fields ($\omega_{ci}\tau_i\gg 1$) the Hall concentration is equal to the sum of the two concentrations. If, for example, the two concentrations are of comparable magnitude, but the mobility of the first is much larger than that of the second one, $\mu_1\gg\mu_2$, the low field Hall concentration equals n_1. At high fields, under the same conditions, the longitudinal resistivity is given by:

$$\rho_{xx}\approx n_2/e\mu_1(n_1+n_2)^2.$$

[a]National Research Council-NASA Senior Research Associate, on leave from the Dept. of Electrical Engineering and Solid State Institute, Technion-Israel Institute of Technology, Haifa 32000 Israel.

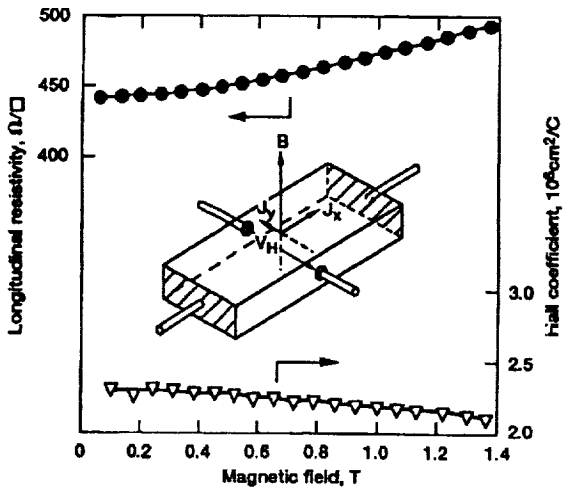

FIG. 1. Theoretical fit to experimental data of longitudinal resistivity ρ_{xx} (circles) and Hall coefficient R_H (triangles) as a function of magnetic field for sample Q12I. Insert shows test configuration.

In our experimental setup we recorded the longitudinal voltage and the Hall voltage continuously versus the magnetic field up to the highest field accessible, 1.4 T. Then, using a nonlinear least-squares method we fitted both sets of experimental data simultaneously to Eqs. (1) and (2). Thus we obtained an estimate of the four variables: n_1, n_2, μ_1, and μ_2. Two problems are faced during this process. First the Hall voltage increases almost linearly with the magnetic field which would result in an improper balance of the computation by underweighting the low field and by overweighting the high field Hall data. To overcome this issue we fitted the Hall coefficient which varies much less with magnetic field. A second problem is present in a simultaneous fitting process when one set of numbers is significantly larger than the other. In this case the latter set would have a marginal effect on the derived parameters. Therefore we introduced a normalization factor. A point in mid-field range was chosen for which the resistivity and Hall coefficient were calculated. The ratio between these figures forms a normalization factor by which the Hall data were multiplied, making these data comparable in magnitude to the resistivity data. Upon completion of the computation the data were renormalized.

Several aspects regarding the accuracy of the procedure were examined. The standard deviation of the parameters derived from the fitting process was found to be better than 0.5%. Second, the procedure was applied to different ranges of magnetic fields to determine the consistency of the results. While the scatter between derived parameters obtained for different ranges was less than 2% at intermediate temperatures (typically between 50 and 200 K), this scatter at higher temperatures may be over 10% in concentration and 5% in mobility. Caution must be taken when choosing the range of fit of the Hall data. Since we fit the Hall coefficient, which is derived from the measured transverse voltage by division with the magnetic field, small errors in the low field data may result in a substantial

TABLE I. Carrier concentrations and mobilities for three samples. Concentrations are in 10^{12} cm^{-2} and mobilities in cm^2/V s.

	300 K						4.2 K	
Sample	n_1	n_2	μ_1	μ_2	n_H	μ_H	n_H	n_{SdH}
Q12H	1.09	3.22	7570	1850	2.80	5080	1.11	0.96
Q12I	1.05	3.17	7710	1920	2.78	5150	1.16	1.01
Q11A	0.557	4.13	8080	1810	2.92	4060	0.624	0.48

deviation of the entire fit. Another source of inaccuracy may be due to the presence of a large transverse voltage at zero field. If the parallel concentration becomes much lower than the 2DEG concentration, the accuracy of the values derived for n_2 and μ_2 may be worse than 10%. This is frequently the case with better samples at the lowest temperatures (and not exposed to light). Under these conditions, $\mu_1 n_1 \gg \mu_2 n_2$, so that the conduction data are dom-

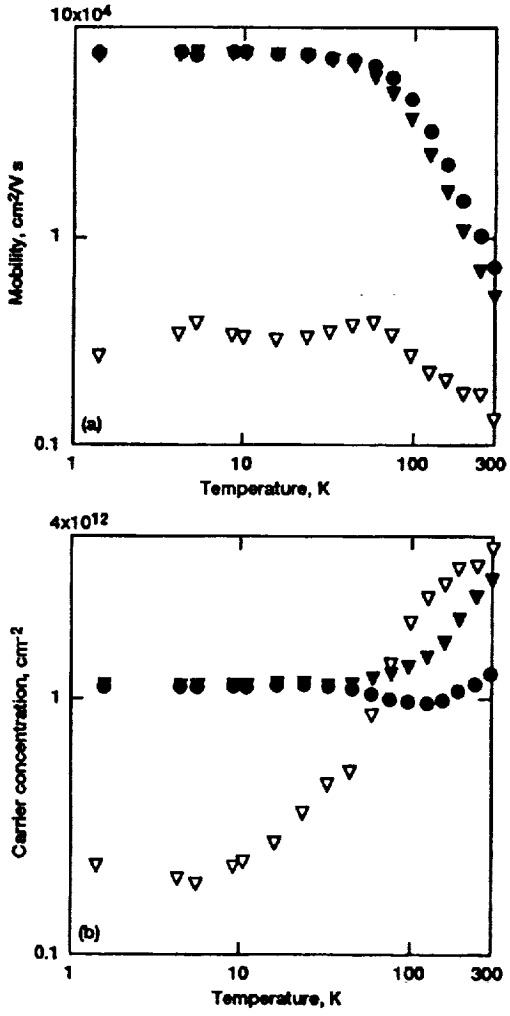

FIG. 2. Hall data and parameters derived from fitting procedure as function of temperature for sample Q12H: (a) carrier concentrations: n_1 (circles), n_2 (empty triangles), and n_H (full triangles); (b) mobilities: μ_1 (circles), μ_2 (empty triangles), and μ_H (full triangles).

inated entirely by the 2DEG carriers. The actual accuracy of the derived 2DEG concentration was evaluated by comparing it to the results obtained from the SdH and Hall experiments performed at liquid helium temperatures.

Table I summarizes the results of the analysis performed on three samples. The samples were MBE grown MOD structures consistent of AlGaAs barrier with 30% Al and a GaAs well. In samples Q12H and Q12I the barrier was delta-doped with Si at a concentration of 3.5×10^{12} cm^{-2}, while in sample Q11A the barrier was homogeneously doped at a concentration of 10^{18} cm^{-3}. Sample Q12I is identical to sample Q12H except that it was removed from the GaAs substrate by an epitaxial liftoff process.[4] The 2DEG concentrations are compared with the concentrations derived from the Shubnikov–de Haas (n_{SdH}) oscillations and the Hall data (n_H) taken at liquid helium temperatures. No second subband population was evident from the SdH data on either sample.

For all the samples examined at room temperature, the derived 2DEG concentration n_1 falls between the measured low-temperature SdH and Hall concentration. The difference between these and the room-temperature Hall concentration is very significant. Altogether the high-temperature Hall data are much closer to that of the parasitic parallel layer. It should be pointed out that this large parallel concentration n_2 is typical for these types of structures. The concentration n_2 drops drastically with temperature and reaches 2×10^{11} cm^{-2} below 50 K. The relatively larger error in room temperature n_1 for sample Q12H is due to a large zero field transverse voltage (0.1 mV with a current of 2 μA). At the lowest field this voltage is more than half of the recorded signal.

Figure 1 shows the experimental points and the results of the fitting process to the data measured at room temperature on sample Q12I. The fit of ρ_{xx} is excellent, while that of R_H exhibits some fluctuations at the lowermost magnetic fields, due to the division by B, as explained before. Even for these points, the error is below 2%.

As an extension of the method we used it to estimate the four parameters n_1, n_2, μ_1, and μ_2 as a function of temperature. Figure 2(a) shows the carrier concentrations and Fig. 2(b) the mobilities as function of temperature for sample Q12H. The low-temperature 2DEG parameters almost coincide with the Hall data because of the low parallel concentration in this temperature range. It is interesting to note that the mobility of the parallel layer μ_2 increases as n_2 decreases with descending temperatures. However, μ_2 remains fairly constant at lower temperatures as might be expected in degenerate semiconductors.

In conclusion we have shown that the simultaneous fit of the magnetic field dependent longitudinal and transverse resistivities can serve as a useful tool in characterization of quantum well structures both enabling room-temperature determination of 2DEG concentration and mobility as well as exploration of the effect of parallel conductance. This may be particularly helpful in better understanding of persistent photoconductivity in these structures.[5]

[1] P. P. Ruden, M. Shur, A. I. Akinwande, J. C. Nohava, D. E. Grider, and J. Baek, IEEE Trans. Electron. Devices ED-37, 2171 (1990).
[2] K. Ploog, M. Hauser, and A. Fischer, Appl. Phys. A 45, 233 (1988).
[3] M. J. Kane, N. Apsley, D. A. Anderson, L. L. Taylor, and T. Kerr, J. Phys. C 18, 5629 (1985).
[4] P. G. Young, R. A. Mena, S. A. Alterovitz, and E. D. Smith, IEEE Trans. Electron. Devices (in press).
[5] S. E. Schacham, R. A. Mena, E. J. Haugland, and S. A. Alterovitz, Mater. Res. Soc. Symp. Proc. 240, 517 (1992).